Atomic force microscopy reveals how relative humidity impacts the Young's modulus of lignocellulosic polymers and their adhesion with cellulose nanocrystals at the nanoscale

Carlos Marcuello, Laurence Foulon, Brigitte Chabbert, Véronique Aguié-Béghin, Michael Molinari

Atomic force microscopy reveals how relative humidity impacts the Young's modulus of lignocellulosic polymers and their adhesion with cellulose nanocrystals at the nanoscale

C. Marcuello[*,1,2], Laurence Foulon[1], Brigitte Chabbert[1], Veronique Aguié-Béghin[1], Michael Molinari[*,2,3]

[1]FARE Laboratory, INRA, Université de Reims Champagne Ardenne, 51100 Reims, France

[2]Laboratoire de Recherche en Nanosciences (LRN), Université de Reims Champagne-Ardenne, 51685 Reims, France

[3]CBMN, CNRS UMR 5248, Université de Bordeaux, IPB, 33607, Pessac, France

carlos.marcuello-angles@inra.fr, michael.molinari@u-bordeaux.fr

Abstract

Lignocellulosic biomass is receiving growing interest as a renewable source of biofuels, chemicals and materials. Lignocellulosic polymers and cellulose nanocrystals (CNCs) present high added-value potential in the nanocomposite field, but some issues have to be solved before large-scale applications. Among them, the interaction between polymers at the nanoscale and the effect of the external parameters on the mechanical properties have to be more precisely investigated. The present study aims at evaluating how the relative humidity affects the reduced Young's modulus of lignocellulosic films prepared with crystalline cellulose, glucomannan, xylan and lignin and how relative humidity changes their nanoscale adhesion properties with CNCs. Using atomic force microscopy and force volume experiments with CNC-functionalized levers, increasing the relative humidity is shown to decrease the Young's modulus values of the different films and promote their adhesion forces with CNCs. In particular, CNCs more strongly interact with glucomannan and lignin than xylan, and in the case of lignin, the oxidation of the film promotes strong variations in the adhesion force. Such results allow to better understand the lignocellulosic film properties at the nanoscale, which should lead to an improvement in the production of new highly added-value composites.

Keywords: cellulose, hemicellulose, lignin, oxidation, adhesion, Young's modulus,

1. Introduction

The development of novel and advanced biobased materials has been shown as a priority to limit the use and dependence on fossil fuels [1]. Material characteristics such as nonhazardous, lightweight, low cost, eco-efficient and available are expected to describe suitable alternatives for sustainability. Resource scarcity and global climate change have recently generated a growing interest in lignocellulosic biomass as a renewable source of biofuels, chemicals and materials [2]. Lignocellulosic biomass, as forests, agroresources and agricultural by products, offers high potential as a sustainable platform to produce a wide variety of chemicals and polymers beyond traditional applications in various fields (packaging, building materials, paperboard, etc.) [3, 4].

Known examples of applications include the combination of plant fibers from different sources with a polymer matrix into composite and/or nanocomposite materials [1] or the use of polysaccharide nanocomposites for new high-value applications [5]. Plant fibers are composed of bundles of highly crystalline cellulosic nano- to microfibers with diameters from 5 nm to 25 µm. The latter structures are embedded by hemicelluloses and lignin with minor amounts of pectin, extractives and ash [6]. The mechanical performance of natural fiber composites depends on the interfacial bonding between not only the fiber surface and the matrix but also the polymers within the fiber cell wall [7]. For ten years, polysaccharide nanocomposites of cellulose nanocrystals (CNCs) have been a promising nanomaterial, due to the excellent optical and mechanical properties of CNCs [8] as well as their homogeneous distribution of sizes [9, 10]. Their large specific surface area (approximately 465 m^2 g^{-1}) provides the potential for interfacial load transfers considerably higher than those achieved with microfibers, thus, enabling a wide range of applications for not only the aforementioned nanocomposites but also advanced materials such as biomedical products, paints, thin films, optical and protection coatings, and electronics [11]. For those different applications, one crucial property of CNCs is their surface chemistry. CNCs are rod-shape particles fully covered by hydroxyl groups. These –OH groups allow the formation of intra- and intermolecular hydrogen bonds, which determine the morphology and reactivity of CNCs. Thus, hydrogen bonding, van der Waals dispersion forces and electrostatic forces are the key noncovalent interactions between CNCs and various polymers, mainly hemicelluloses in plant fibers [12] and bioinspired hydrogels and films [13], lignin and polyelectrolytes in antireflective and anti-UV transparent films [14, 15]. Moreover, the reactivity of hydroxyl moieties allows the covalent

grafting of CNCs thanks to numerous chemical processes, as described in the literature [16]. Thus, understanding the interaction between CNCs and other lignocellulosic polymers is a topic of broad interest for developing new biobased and sustainable nanocomposites. Indeed, the final properties of such materials strongly depend on the structure of the polymers involved and on the strength of the bonds formed between them, which directly impact the mechanical properties of the final products.

In addition to the structure and intrinsic properties of lignocellulosic materials, external parameters also play a key role in the final performance of the nanocomposites. Indeed, the physicochemical properties of lignocellulosic materials depend on the relative humidity of air and the hygroscopic behavior of the polymers. For example, hydrophilic polymers as hemicelluloses can uptake a high amount of water molecules, especially under high relative humidity (RH) conditions, compared to that of hydrophobic amorphous lignin and crystalline cellulose [17]. As a consequence, RH variations can lead to changes in the polymer structure, thus, modifying the physico-chemical, mechanical, and barrier properties of the arising composite films that could impact their functionality and future performance [18]. Indeed, an increase in relative humidity can promote the swelling effect due to the uptake of water molecules by lignocellulosic polymers [17, 19, 20] thereby inducing changes in their mechanical properties, as shown by experimental studies and atomistic simulations [20-22]. The sorption of water molecules can induce changes in macromolecular conformation and noncovalent interactions such as hydrogen bonds between polymer chains. The impact would be even more complicated for complex assemblies such as nanocomposites made of crystalline cellulose and amorphous polymers such as lignin and hemicellulose. It is then of prime importance to initiate relevant experiments to study at a small scale the RH variation in mechanical properties, such as the adhesion or the Young Modulus (YM), of lignocellulosic films.

Different biophysical techniques, such as a quartz crystal microbalance (QCM) or surface plasmon resonance (SPR), can be used to obtain relevant information on the interactions between cellulosic, hemicellulosic, or lignin-based polymers [23, 24]. However, these are indirect methods for adhesion force measurements and only work at the liquid/solid interface. Moreover, some effects, such as population heterogeneity, crowding effects, transient phenomena, among others, can be typically hidden in the measured average value [25]. For this reason, nanoscale techniques, such as atomic

force microscopy (AFM), are desired to measure nanomechanical properties. AFM is a technique where the probe, usually a sharp tip, interacts with an external sample surface to map the topography of a sample with nanometric resolution. In addition to determining the topography by performing force-distance curves, it is also possible to achieve quantitative measurements of the YM or to measure the interaction between individual biomolecules. Quantitative nanomechanical modes are now commonly used for different systems, including CNCs and lignocellulosic films [26-29] and allow to get reliable measurements of the nanomechanical properties. Nevertheless, to perform adhesion force measurements with functionalized tips, Force-Volume (F-V) experiments are still preferred[30, 31]. Such experiments are allowed by covalently attaching the biomolecule of interest to a tipped/tipless AFM lever and then measuring the adhesion forces involved between the tip and the sample. Many systems including protein unfolding, antibody/antigen, streptavidin/biotin or even cellulose/hemicellulose [32] have already been studied. The main issue with adhesion measurements is linked to the tip or lever functionalization, which remains difficult, especially for cellulosic and lignocellulosic polymers. Many chemical procedures using linker molecules have been developed [33], but in regard to functionalization with CNCs (for instance, by using such protocols), unreacted linker molecules can interfere during the SMFS data acquisition. To overcome this limitation, Langmuir-Blodgett (LB) technology has been reported as a suitable method to attach cellulose in the form of rod nanoparticles (CNCs) and with a controlled coverage [34].

In this study, AFM and its related nanomechanical modes were used to investigate the effect of RH on the YM of model films based on lignocellulosic polymers (CNCs, hemicelluloses (glucomannan and xylan), lignin and oxidized lignin) and on the adhesion values between these films and CNCs. Thanks to the controlled CNC coverage of an AFM lever, precise adhesion measurements were performed at different RHs, and the impact of variations in the film YM on the adhesion properties was investigated. The quantification and characterization of the intermolecular forces driven at the nanoscale level represent a preliminary step towards promoting the design of new fully biosourced and performant composites using lignocellulosic polymers.

2. Experimental procedures

2.1 Materials

Reagents and analytical-grade solvents were used following the indications of the manufacturer. Dioctadecyldimethylammonium bromide (DODA) and sodium hydroxide (NaOH) were supplied from Sigma Aldrich, France.

2.2 Film preparation

CNCs films: CNCs were prepared from bleached ramie (*Boehmeria nivea*) fibers (Stucken Melchers, Germany). Small fragments were treated with a solution of 2 % NaOH (w/v) at 20°C for 48 h before performing hydrolysis overnight with 65 % (w/w) H_2SO_4 at 35°C under constant stirring. The resulting suspensions were washed with water until neutral pH and dialyzed using a 6 000 molecular-weight-cutoff regenerated cellulose membrane. The resulting CNC suspensions were diluted to an appropriate concentration, sonicated for several mins using a Sonics vibra-cell (750 W, Fisher-Bioblock, France) and stored at 4°C before use. The mean value crystal dimensions (section of 5-6 nm and length of 130 nm ± 50 nm) were estimated from AFM images by statistical analysis of the cross section profiles on single rods of dilute nanocrystal suspensions deposited on a silicon wafer [35]. CNC films were prepared by casting the mixtures in glass Petri dishes via pouring 2.25 mL of 1.8 % CNC and incubating at room temperature overnight.

Hemicellulose films: Konjac glucomannan (GM, low viscosity, Megazyme) and xylan (XYL) isolated from oat spelt [17] were suspended in water/ethanol absolute grade (97:3, v/v) before heating at 100 ºC with mild stirring until complete solubilization (15-20 min). The solution was cooled to room temperature, and the volume adjusted with water to obtain solutions of 10 g/L (w/v). The solutions were centrifuged at 10 000 revolutions per minute (rpm) for 10 min at room temperature. The stock solutions were stored at 4 ºC before use. GM and XYL films (30 µm ± 2 µm) were prepared by casting stock solutions in a Petri dish or in a rotating Teflon tube under a nitrogen flux, respectively, at ambient temperature for 24 h.

Lignin films: Lignin was isolated from maize stalks (*Zea mays L.*) using a mixture of dioxane and 0.2 M hydrochloric acid (9/1 v/v), according to the procedure described by

Monties [36]. The chemical and structural characteristics were detailed in a previous work [37]. Lignin was dissolved at 10 g/L in aqueous dioxane (9/1, v/v), and 30 µL of this solution was spin-coated onto a silicon wafer (slide of 1 cm^2) using a commercial spin-coater (Speedline Technologies, USA) at 4 000 rpm. Prior to coating, the silicon wafer was cleaned in a freshly prepared Piranha solution for 30 min., rinsed with ultrapure water exhaustively and placed in a jar for silanization with APTES (3-aminopropyltriethoxysilane, Sigma-Aldrich, France) in the vapor phase for 3 h after the elimination of ambient air. The lignin-coated wafer was then dried by heating under vacuum at 70°C for 1 h to drive off the dioxane. In the particular case of lignin films, knowing that lignin is sensitive to the oxidation, an oxidative pretreatment was performed by laccase-oxidized ABTS to increase the stability of the film by the oxidation of phenolic groups to quinones without a detectable change in the molecular weight distribution [33]. Some of lignin-coated wafers were treated with 1 mM oxidized ABTS (2,2'-azinobis (3-ethylbenzethiazoline-6-sulfonate, Sigma-Aldrich) via incubation with laccase from *Pleurotus ostreatus* (E.C 420-150-4, Sigma-Aldrich) according to Kent's method. Following the treatment, the samples were rinsed thoroughly with ultrapure water (resistivity of 18 mΩ.cm) and dried before AFM and force volume measurements. The thicknesses of the native lignin (LIG) and oxidized lignin (OX-LIG) films were determined by spectroscopic ellipsometry rendering similar thickness of 57.0 ± 0.9 nm.

2.3 Langmuir-Blodgett functionalization of CNCs

Tipless AFM levers were treated with a UV-ozone exposure (Bioforce Nanosciences, USA) for 30 min before their use to expose the silicon dioxide chemistry (SiO_2). The LB technology was exploited as reported elsewhere [34]. A DODA chloroform amphiphilic solution (1 mg. mL^{-1}) was spread on the CNC suspension (0.05 %, w/v) freshly prepared and poured into a KSV mini-trough [KSV Technology, 75 x 330 mm minitrough, Finland] [35]. The surface pressure (π, mN/m) was monitored using a Wilhelmy balance to control the formation of the CNC layer at the air/water interface. Three values of π were defined to transfer the CNC layer onto the AFM levers at three different densities (5, 15 and 30 mN/m). The film compression and further vertical dipping rates were fixed at 2.0 mm/min and 0.1 mm/min, respectively, with a constant temperature of 25 ± 1 ºC. Finally, the remaining DODA molecules were eliminated with

subsequent chloroform, dilute NaOH and MiliQ water washes (3 x 5 min) [11]. The functionalized AFM tipless levers with CNCs were stored under a protected atmosphere until their use.

2.4 Atomic Force Microscopy

All experiments were performed with a Multimode-8 AFM setup from Bruker (Santa Barbara, CA, USA). The different experiments, including adhesion measurements, were willingly performed in air. Indeed, as the objective of the study was to mimic the interaction between lignocellulosic polymers for application in composite materials, the proper medium is the ambient environment. Furthermore, measurements in aqueous media could lead to wrong results as the water could change the structure of the different lignocellulosic films and even dissolved them. To be as close as possible of the applications, the RH was the key parameter that was changed during the measurements. A specific setup was mounted to precisely control the RH during all the AFM experiments. A sealed chamber was used to isolate the AFM head, and the RH inside the chamber was controlled by a Wetsys system (Setaram Instrumentation, France). A Tynytag device (Gemini Data Loggers, UK) monitored the RH for all image acquisitions with a negligible error for the whole setup of 0.3 % RH. RHs of 15, 45, 65, and 95 % were used for the different experiments. Topography AFM images were acquired using PeakForce tapping mode in air [38-41]. This operational mode benefits of the accurate control of tip-sample interaction forces measured by the bending of the AFM cantilever, preventing lateral forces due to intermittent contact with the sample. Continuous force-distance curves were executed at a constant frequency of 1 kHz enabling acquisition rates from 0.7-0.9 Hz.. Silicon ScanAsyst air triangular levers with a nominal spring constant of 0.4 N/m (Bruker Probes, USA) and ultrasharp tips (a nominal tip radius of curvature of 2 nm) were used for topography measurements. Representative AFM images of 5 µm x 5 µm from each lignocellulosic film were analyzed by using the root mean square roughness parameter (Rq). The Rq parameter was measured for at least three representative AFM images that came from different areas of each film, and at least three different samples for each film were studied. The resolution of all AFM images were of 512 x 512 data points All raw images were rendered using Nanoscope analysis 1.8, with exception to quantitative determination of

the coverage of CNCs on AFM levers which has been performed with Gwyddion [42] software.

The reduced YM was determined for all the films using the Peak Force Quantitative Nanomechanics (PFQNM) mode of the AFM. This mode displays a force-distance curve at each image pixel, and the treatment of the curves allows the measurement of a reduced YM for each pixel. For the PFQNM measurements, AFM TAP525 tips were used (Bruker probes, USA) with a nominal spring constant of 200 N/m and a nominal resonance frequency of 525 kHz. The vertical AFM probe oscillation frequency was 1 kHz. The high nominal spring constant of 200 N/m was in consonance with the expected YM previously reported on the order of a few GPa [28]. The deflection sensitivity was calibrated by running force-distance curves on a clean hard sapphire surface in at least 3 different areas to obtain an average value. The feedback loop was adjusted using the Sync distance parameter calibrated on a sapphire surface provided by Bruker. The AFM lever spring constant was estimated using the Sader method [43]. The tip radius was determined by scanning a sharp-edged titanium roughness sample (model RS-15M, Bruker Probes, USA). The tip radius was tested before and after each measurement to visualize potential broadening effects that might have occurred during image acquisition [44]. The applied force was 200 nN. To extract the reduced YM, mainly three models exist, the Hertz [45], the Johnson, Kendall and Roberts (JKR) [46] and the Derjaguin, Muller and Toporov (DMT) [47]. Regarding the characteristics of the tips and the adhesion properties of the different films, the more appropriate model is the DMT (eqn. 2); it takes into account the role of van der Waals forces that act along the contact area perimeter, being not negligible for sharp tips.

$$F = \frac{4}{3} E^* \sqrt{R^* i^3} + F_{adh} \quad (2)$$

where F is the applied force, i is the indentation depth, F_{adh} is the adhesion force of the AFM tip from the substrate surface, and R^* is the reduced radius that is correlated with the AFM apex tip radius ($R_{indenter}$) and the radius of the measured surface ($R_{surface}$) (eqn. 3).

$$\frac{1}{R^*} = \frac{1}{R_{indenter}} + \frac{1}{R_{surface}} \quad (3)$$

where E^* is the reduced elastic modulus, which serves to calculate the YM from the sample of interest (E) (eqn. 4).

$$\frac{1}{E^*} = \left(\frac{1-\nu^2}{E} + \frac{1-\nu_{tip}^2}{E_{tip}} \right) \quad (4)$$

including the modulus of the tip (E_{tip}), and the Poisson ratios (ν and ν_{tip} for sample and tip, respectively). According to previous work on plant cell walls, ν is defined as 0.3 [48]. We considered the use of E^* to be more accurate, given the anisotropic composition of cellulose [49]. For the PFQNM mapping of each film, a scan size of 5 µm x 5 µm was defined. Mappings of 512 x 512 pixels were performed at a scan rate of 0.4 Hz. At least three different films for each type of polymer and three areas for each film were studied. All pixels from the DMT channels were taken into consideration for the analysis of each image, allowing for more than 500 000 analyzed curves for each YM measurement. The final average YM value was deduced from the maximum of the Gaussian distribution associated with the measurements [28]. Typical YM distribution are shown in **Fig. SI 2** for different humidities. The R^2 parameter of each distribution was systematically calculated for each distribution and superior to 0.9.

For the adhesion measurements, the functionalized levers (as described in a previous paragraph) were used. Three different coverages of CNCs on the AFM lever (17.6 ± 5.5 %, 32.8 ± 6.9 % and 55.8 ± 5.5 %) were used in this study corresponding to 3 different values of π (5, 15 and 30 mN/m). A typical image showing the lever prepared at 15 mN/m is shown in Fig. SI 1 and the full procedure to characterize the different functionalized AFM levers could be found in [34]. The deflection sensitivity and spring constant of the AFM levers functionalized with CNCs were acquired as previously described. The functionalization has a negligible effect on the spring constants of the levers with values varying from 0.388 to 0.395 N/m whatever the CNC coverage. As preliminary experiments have shown that the adhesion forces between then CNCs and the different lignocellulosic polymers were not rate dependent, the small variation of the spring constant does not affect the measurements. The intermolecular forces between lignocellulosic films and AFM levers functionalized with CNCs by LB at 3 different values of π (5, 15 and 30 mN/m) were determined for increasing values of RH (15, 45, 65 and 95 %). As the capillary forces between the functionalized AFM tip and the external sample surface can depend on several parameters such as contact angle, size of the object, temperature [50] and RH [51], all the parameters were kept constant except

the RH. Unmodified AFM levers were also tested as negative control on the lignocellulosic films for the same values of RH showing no specific adhesion (**Fig. SI 5**). The experiments were carried out with the same equipment described above, working in Force-Volume mode (F-V) in air. F-V allows for real-time mapping of local areas providing quantitative adhesion forces between the functionalized AFM lever and the external substrate surface. The topography and adhesion force maps were acquired simultaneously. As with the previous AFM experiments, at least three samples for each polymer were studied, and three different areas were scanned on each sample. Representative areas with scan sizes of 5 µm x 5 µm and 2 µm x 2 µm are shown in the paper. The forward and reverse tip velocity was fixed at 636 nm/s for all films. All SMFS measurements were defined at 48 pixels per line, allowing for more than 2 300 force curves in each image. All AFM analysis of the lignocellulosic films were performed after 2 h at each RH. This aspect serves to ensure that the lignocellulosic films have reached the equilibrium state given to previous work on sorption isotherms [17]. The topography of each of the three functionalized AFM levers was recorded before and after F-V mapping to check that the CNCs remained attached and maintained their integrity. The mean rupture force values were obtained by plotting histograms fitted by Gaussian distributions as the typical ones shown in **Fig. SI 5**. For each distribution the R^2 parameter was calculated and was generally superior to 0.90 except for scattered data as we observed for force-distance curves of unmodified AFM levers (**Fig. SI 7**). To serve as a control, unmodified AFM levers were also tested in the same conditions than CNC-functionalized AFM levers. The adhesion forces of unmodified AFM levers with lignocellulosic films were significant greater than with CNC-functionalized levers due to a higher load contact area between both surfaces (**Fig. SI 6**). The force distributions were broad and difficult to be fitted by Gaussian equation (**Fig. SI 7**) showing unspecific interactions.

3. Results and discussion

3.1 Characterization and morphology study of the different lignocellulosic films at different RHs

The topographies of the different films were acquired to analyze their morphologies. Topography AFM images provide three-dimensional information (x, y and z) including the roughness values of the films. Representative AFM images from CNC,

glucomannan (GM), xylan (XYL), lignin (LIG) and oxidized lignin (OX-LIG) films at 45 % RH are depicted in **Fig. 1**. The morphology of CNC rods was found to be similar to what has been previously described [34], where the mean values of length and height were 180.9 ± 12.5 nm and 6.3 ± 0.4 nm, respectively (**Inset, Fig. 1 A**). GM films showed long filaments on their surface (**Inset, Fig. 1 B**). These fiber features have been previously observed by electron microscopy and AFM [28, 52]. In contrast, XYL did not exhibit these structures (**Inset, Fig. 1 C**), as previously described [28]. LIG films displayed randomly distributed nodules (**Inset, Fig. 1 D**) [15]. Finally, although the OX-LIG films displayed a similar nodular morphology, some cracks could be observed. (**Inset, Fig. 1 E**). The root mean square (Rq) parameter was calculated for each film at 45 % RH (**Fig. 1 F**). The XYL film presented the highest value of Rq with 23.6 ± 1.8 nm, followed by OX-LIG, LIG, GM and CNC films (20.1 ± 1.7 nm, 10.0 ± 0.5 nm, 9.1 ± 0.7 nm and 6.2 ± 0.2 nm, respectively). On average, the Rq roughness values obtained for LIG films (10.0 ± 0.5 nm) were higher than previous values reported for lignin isolated from spruce, wheat straw and eucalyptus (5.4 ± 0.2, 4.2 ± 0.1 and 2.1 ± 0.1 nm, respectively) [53]. This variation can be due to the morphology of the LIG features, which is dependent on the lignin source and method of isolation, as well as the techniques used in the film preparation. OX-LIG nodular features show higher heights (**Fig. 1 G**) in comparison to LIG layers (**Fig. 1 H**). We hypothesize that this observation is based on the expansion produced when the nodular lignin features crack after oxidation process (**Fig. SI 2 A**). The evolution of the roughness of cellulose/hemicellulose/lignin films was also monitored in the RH range from 15 to 95 % (**Table 1**). Negligible modification of the Rq parameter was observed for XYL, LIG and OX-LIG films; the Rq variations are lower than 0.1 % for XYL, 1.0 % for LIG, 0.5 % for OX-LIG, 3.2 % for CNC and 5.6 % for GM films. Further analyses of the nanomechanical properties of the different films is required to discern whether they are affected by RH.

3.2 Effect of relative humidity on the reduced YM of cellulose/hemicellulose/lignin films.

The reduced YM values of the cellulose/hemicellulose/lignin films were determined at RH varying from 15 to 95 %. At RH of 45 %, the reduced YM values of CNC, GM, XYL, LIG and OX-LIG were 10.3 ± 0.9 GPa, 5.1 ± 0.4 GPa, 6.4 ± 0.2 GPa,

6.3 ± 0.4 GPa and 11.0 ± 1.6 GPa, respectively (**Fig. 3**). Under this environmental condition, the reduced YM values of OX-LIG and CNC films were higher than those of the remaining lignocellulosic films. This observation can be related to the nature of each film; CNCs presented highly crystalline rods, while the OX-LIG film showed entangled nodular features.

Representative images of the DMT maps from these films obtained by increasing the RH are shown in **Fig. 2**. The reduced YM values of CNC, GM, XYL, LIG and OX-LIG films at different RHs are depicted in **Fig. 3**, indicating the formation of a homogeneous distribution of each polymer at the film surface shown in the topography images (**Fig. 1**). For all plant cell wall polymers, the reduced YM of the films decreased with increasing RH values. However, the extent of variation between RH 15 and 95 % for CNC (from 10.9 GPa to 9.2 GPa, 15.6 % decrease) and LIG films (from 6.7 GPa to 5.8 GPa, 13.4 % decrease) was considerably weaker than that for XYL (from 7.6 GPa to 5.1 GPa, 32.9 % decrease), GM (from 9.4 GPa to 4.3 GPa, 54.2 % decrease) and OX-LIG (from 13.8 GPa to 6.5 GPa, 52.9 % decrease) films (**Fig. SI 3**). The rather weak sensitivity of CNC films to increasing relative humidity can be explained by the crystal structure of the nanocrystals and the high aspect ratio of CNCs causing more points of contact with other surrounding rods. These two physical characteristics produce two main effects: i) greater reduced YM values due to the high compaction of CNC nanorods inside the film and ii) lower water adsorption and/or immobilization of water molecules probably due to the existence of some hydrophobic faces of cellulose nanocrystals exposed to air [54] or of fewer interstitial voids between CNC rods (as shown for CNCs films [17]).

The reduced YM values for GM and XYL hemicellulosic films (5.1 ± 0.4 GPa and 6.4 ± 0.2 GPa at 45 % RH, respectively) are in accordance with that of previous studies [22, 28, 55, 56]. The GM and XYL films exhibited strong decreases (54.2 % and 33.0 % respectively) in the reduced YM between 15 % and 45 % RH. It is known that hemicelluloses are polymers capable of high moisture sorption in comparison with other plant cell wall polymers [17, 20]. Thus, the difference between GM and XYL reduced YM values (9.4 ± 0.6 GPa and 7.6 ± 0.3 GPa, respectively at RH 15 %) can be explained by the difference backbone substitutions (20 % arabinose for XYL and less than 5 % for GM) as well as by their different molecular weights (45 kDa and 60 kDa for XYL and GM, respectively) [17] inducing different intramolecular interactions

between the chains. In addition, GM contains three –OH moieties per glucose/mannose unit, whereas XYL only retains two hydroxyl groups per xylose monomer. Therefore, more water molecules can interact with GM than with the XYL polymer. Moreover, XYL contains a weak amount of residual lignin (4 %) [17], which can be exposed at the outer surface during film preparation. This residual lignin can interact physically and covalently with the xylan backbone, yielding a tight lignin-carbohydrate network [6] to provide a barrier against water.

In the case of the LIG films, increasing RH did not have significant impact on the reduced YM (6.7 GPa and 5.8 GPa from 15 to 95 %, 13.4 % decrease). This result is in agreement with a recent study on the hygromechanical properties of lignin [57] and can be attributed to the hydrophobic nature of lignin, which can hinder the penetration of water into the inner structure of lignin nodules [57-59]. However, the OX-LIG films displayed a very distinct pattern. The first difference involved the elastic modulus, which for OX-LIG (13.8 ± 1.5 GPa) was twice that of the LIG films at 15 % RH (6.7 ± 0.5 GPa). Such an observation can result from the formation of cross-linked lignin structures by laccase-oxidized ABTS [60]. Accordingly, the formation of an oxidized lignin network has been shown to enhance the tensile strength and mechanical properties of colloidal materials [61]. Moreover, the mechanical properties of OX-LIG films were drastically reduced with the increase in RH (from 13.8 ± 1.5 GPa to 6.5 ± 0.6 GPa for 15 to 95 % RH), which was in contrast with the behavior of the LIG films. This behavior is not due to change in the structure of the OX-LIG with RH increase as the rugosity and the topographic features remain the same with the RH increase (Table 1). As mentioned previously, the lignin network formed by the oxidation of the film surface exhibit more cross-linkage between monomer units, with nodular structures connected between them as 2D coil structures (**Fig. SI 2**). One difference between the LIG and OX-LIG films is the fact that some cracks are appearing in the nodule surfaces and thus, it could be assessed that when the RH is increasing, water molecules could penetrate to the inner OX-LIG substrate through the cracks. As water acts as a plasticizer of lignin, it explains the decreasing mechanical properties. Notably, the reduced YM is lowered near the cracked areas due to the water uptake (**Fig. SI 2 B**). For all cellulose/hemicellulose/lignin films, we observed the Rq roughness parameter as not having a significant influence on the reduced YM. However, the RH can not only influence the reduced YM of analyzed cellulose/hemicellulose/lignin films but also the

adhesive properties between the films and CNC-functionalized AFM levers. A thorough analysis of how RH impacts the interactions of CNCs with the rest of lignocellulosic polymers is shown.

3.3 Effect of relative humidity on the adhesion properties between CNC-functionalized AFM levers and the different films.

The intermolecular interactions between CNCs and pure cellulose/hemicellulose/lignin films were assessed at the nanoscale using LB to functionalize CNC rods on AFM levers. The AFM levers functionalized with CNCs at π = 15 mN/m were used and provided 32.8 ± 3.4 % coverage of CNCs on the AFM lever [34] (**Fig. SI 1**). The coverage percentage was expressed as the surface of the external face of CNC rods per unit of AFM lever area. Although coverage of the AFM lever was precisely controlled, SMFS experiments under air conditions can be affected by capillary forces [62]. This phenomenon occurs when a water meniscus between both surfaces forms by the condensation of air humidity [63]. Indeed, RH can affect molecular bio-recognition by promoting hydrogen bond formation, and thus, adhesion forces between an AFM probe and substrate, which is pronounced for polar polymers (such as lignocellulosic components). Knowing that moisture also enhances the hydrogen bonding between both materials of interest [64], the effect of RH on the intermolecular forces between CNCs and cellulose/hemicellulose/lignin films was then examined. **Figure 4** shows the maps corresponding to the topography and the adhesion forces between CNC-functionalized AFM levers and the CNC, GM, XYL, LIG and OX-LIG films at 45 % RH. Representative force-distance curves for CNCs with the cellulose/hemicellulose/lignin films are displayed in **Fig. SI 4**. Comparing the different polymer films, the results show that adhesion forces between CNCs:GM and CNCs:LIG are stronger than CNCs:CNCs, CNCs:XYL and CNCs:OX-LIG (25.7 ± 2.6 nN, 24.9 ± 8.4 nN, 8.4 ± 0.5 nN, 8.8 ± 4.8 nN and 8.4 ± 2.2 nN, respectively at RH of 45 %, **Table 2**). Relative SD of adhesion forces is higher for XYL, LIG and OX-LIG substrates (54.5 %, 33.7 % and 26.2 %, respectively at RH of 45 %) in comparison with CNC and GM films (6.0 % and 10.1 %, respectively at RH of 45 %), which could be explained by the high roughness of these films compared to CNCs and GM (**Table 1**) and nodular morphology. Surface geometry and roughness play a key role in the adhesion force measurements and influence on the adhesion distribution [65].

From these results, two distinct groups of lignocellulosic polymers differ from each other: one with strong intermolecular adhesion forces with CNCs (between 20 and 35 nN) for GM and LIG films, and second with weaker intermolecular adhesion forces (between 7.5 and 12.5 nN) for CNC, XYL and OX-LIG. These data are consistent with previous work reporting strong interactions between konjac glucomannan and cellulose [66]. Tensile strength, thermal stability, as mechanical properties are improved when GM is blended with cellulose [67]. Concerning LIG films, the highly hydrophobic nature of this polymer may promote the formation of ultrathin water layers at their external surface. Water molecules could have detrimental effects on force volume experiments directly interacting with the CNCs attached on AFM levers. That could explain the high interaction between CNCs and LIG. In contrast, the situation differs with OX-LIG. The laccase-oxidized ABTS pretreatment induces a decrease in the content of phenolic OH groups, meanwhile increases the content in carboxylic groups [68, 69]. These modifications seem to induce a decrease in adhesion forces between CNCs and OX-LIG. Moreover, the other detrimental factor at the expense of stronger interactions with CNC-functionalized AFM levers is the high roughness of OX-LIG films (**Fig. 1 F**). The second example of weak interactions is CNCs:XYL film which is in agreement with previous study reporting that XYL is not as closely associated with cellulose as GM in plant [12]. XYL used in our study contained a weak percentage of nonpolar phenolic compounds, which may prevent formation of hydrogen bonds if they are located at the external film surface. Finally, CNCs:CNCs intermolecular adhesion forces revealed to be weaker in air environment compared to CNCs interactions with LIG and hemicelluloses films. It was expected to observe higher adhesion force values due to the large number of potential hydrogen bonds that can be formed between CNCs [70]. Short-range repulsive steric forces seems to dominate the interaction between CNCs:CNCs surfaces due perhaps to the presence of ester sulfate groups negatively charged at CNC surface (0.7 % w/w), even in the controlled humidity of the AFM chamber, rendering the electrostatic and van der Waals bonds less important [71]. This fact is due to hydrogen bonds based on permanent dipoles due to the significant difference of electronegativity between the atoms which form the bond, while electrostatic and van der Waals interactions the dipoles are temporary and thus, making weaker and short-lived interactions. Other feasible explanation could be related to the crystal structure of CNCs [28].When an external force is exerted by the functionalized

AFM probe, CNCs from the film will suffer minor degree of deformation than the other studied amorphous polymers, being thus no able to make contact with the lateral faces of the CNCs rods which are present on functionalized AFM lever.

Once the impact of RH on adhesion properties at defined coverage of CNC-functionalized AFM levers have been analyzed and show how their interaction with cellulose/hemicellulose/lignin films increases with RH. This observation is in agreement with larger number of hydrogen bonds formed between both surfaces at high values of RH. Now, we will focus on the effect of the CNCs coverage on intermolecular interactions with cellulose/hemicellulose/lignin films modifying the contact area between both surfaces.

3.4 Impact of CNCs coverage on the interaction with the different films

Finally, the effect of CNCs coverage on functionalized AFM levers on adhesion properties with cellulose/hemicellulose/lignin films is also addressed at several values of RH. Functionalized AFM levers with CNCs coverage of 17.6 ± 2.7 %, 32.8 ± 6.9 % and 55.8 ± 2.6 % were prepared by LB at π of 5 mN/m, 15 mN/m and 30 mN/m, respectively [34]. As a general trend the data show that for all complexes, adhesion forces were greater working with functionalized AFM levers with upper values of π whatever was the CNCs coverage of AFM lever (**Fig. 5**). Comparing the different polymer films, the results show that adhesion forces between CNCs:GM and CNCs:LIG are stronger than CNCs:CNCs CNCs:XYL and CNCs:OX-LIG at 45 % RH for CNC-functionalized AFM levers with a π of 5 mN/m; similar to what was previously shown, higher values were obtained using a lever functionalized at 15 mN/m. The adhesion forces increased up to 14.7 ± 1.5 nN, 42.6 ± 4.1 nN, 11.4 ± 2.5 nN, 48.0 ± 17.5 nN and 16.8 ± 4.8 nN when using the AFM lever functionalized at a π of 30 mN/m. In addition, increasing the air RH induced significant changes in the intermolecular adhesive interactions using AFM levers functionalized with a high CNC coverage (a π of 15 mN/m and 30 mN/m), whereas similar force values were achieved at a low CNC coverage (a π of 5 mN/m). This phenomenon can be interpreted as the global contribution of the external and lateral sides of CNC rods when the polymer complex takes place. The quantity of available CNC lateral and outer sides was significantly higher in the case of the AFM lever functionalized at a π of 30 mN/m. These results are in agreement with recent data on hemicellulose films [34] and provide new insights on

CNCs:CNCs, CNCs:LIG and CNCs:OX-LIG intermolecular interactions. The relative SD of the adhesion force maintained similar values for the tested CNC-functionalized AFM lever at a π of 5 mN/m (13.0 %, 6.0 %, 8.8 %, 5.8 % and 13.0 % for CNC, GM, XYL, LIG and OX-LIG films, respectively at RH of 45 %). The relative SD reached 10.2 %, 9.6 %, 21.9 %, 36.4 % and 28.6 % for the same substrates when a CNC-functionalized AFM lever at a π of 30 mN/m was used at the same aforementioned value of RH. AFM levers with less coverage of CNCs expose less points of contact with the cellulose/hemicellulose/lignin substrate, which minimizes not only the adhesion between both surfaces but also the SD force distribution. All data regarding CNC-functionalized AFM levers by LB at a π of 5 mN/m and 30 mN/m are recorded in **Table 2**.

3.5 Relation for the reduced Young modulus vs adhesion forces

To conclude, RH leads to a decrease in the YM of cellulose/hemicellulose/lignin films to different degrees depending on the nature and structural state of the plant cell wall polymer and promotes adhesion forces between CNCs and the other polymers. To evaluate the relation between the reduced YM of a film and its adhesion properties with CNC-functionalized levers, the case of LIG and OX-LIG films at different RHs is illustrated (**Fig. 6**). A high coverage of CNCs (π = 30 mN/m) enabled discrimination of the interactions between CNC-functionalized AFM levers and both lignin films. From RH 15 to 95 %, the LIG film showed a small decay in the reduced YM (from 6.72 GPa to 5.79 GPa, -13.8 %), but it showed increase interactions with the CNC-functionalized AFM lever (from 43.6 nN to 54.0 nN, +23.8 %). The thickness of the water layer deposited on the LIG film might have been greater at high RH, thus, causing greater adhesion force events between both surfaces. The elastic deformation of the LIG film at high RH could promote the interaction between the LIG film and the lateral CNC rod faces. On the contrary, when the RH ranged from 15 to 95 %, the OX-LIG film displayed a significant decrease in the reduced YM (from 13.8 GPa to 6.5 GPa, -52.9 %), whereas a constant increase in adhesion forces (from 15.8 nN to 17.1 nN, 8.2 %) was evident. These findings suggest that the relation between Young's modulus and adhesion forces according to RH can be changed after simple oxidation of lignin by ABTS. We can hypothesize that either the oxidation makes lignin more sensitive to water in the core of nodules with some change in the distribution of chemical groups on

the surface which induce increase in Young's modulus without change in adhesion properties in the studied RH range. High-level water uptake was already observed after the oxidative reaction by Fenton's reagent of films made of cellulose and lignin [37, 72]. Thus, the change in adhesion properties on OX-LIG in comparison with that on the LIG film can yield important applications for the production of nanocomposites with novel properties [61].

Finally, an overview of how the variation in the effect of RH impacted the YM values of the lignocellulosic polymers and the adhesion forces using CNC-functionalized AFM levers at a π of 5 mN/m, 15 mN/m and 30 mN/m is shown in **Fig. SI 8**. When the coverage of CNCs on the AFM lever was low (17.6 ± 5.5 % at a π of 5 mN/m), no strong relation existed between the adhesion forces and YM values of the films. This fact is linked to the low differences in intermolecular forces formed between both surfaces. At higher coverages of CNCs on the AFM lever (32.8 ± 6.9 % and 55.8 ± 5.5 % at a π of 15 and 30 mN/m, respectively), two regions exist where it is possible to discriminate the films studied. As previously shown, the LIG and GM films were located at the upper region in their opposition with cellulose, while the XYL and OX-LIG films where are placed at the lower region of **Fig. SI 8**. Thus, it is important to point out that controlling the coverage of the polymer of interest on the functionalized AFM lever is a key factor when addressing interactions with the analyzed lignocellulosic films.

4. Conclusions

Here, we studied the impact of RH on the adhesion properties between five lignocellulosic films (GM, XYL, CNCs, LIG and OX-LIG) and AFM levers functionalized with different coverages of CNCs and how RH affects to the reduced YM of these films. The reduced YM of the lignocellulosic films are impacted by increasing the RH. The variation in the reduced YM with respect to RH is more remarkable for the GM, XYL and OX-LIG films, which is in agreement with the water sorption capacities of these polymers. However, strong differences are observed between the LIG and OX-LIG films. The LIG film better conserves the YM property with varying RH, proving to be an excellent moisture barrier. In the case of OX-LIG, the morphology of its nodules, where extensive cracked regions are observed, could serve as a trigger factor to induce water uptake in this film. Moreover, the interaction

forces between AFM levers functionalized at different coverage of CNCs and cellulose/hemicellulose/lignin films at different RH were measured. We provide evidence that CNCs partake in stronger interactions with the LIG and GM films with respect to CNC, XYL and OX-LIG substrates. The increase in RH promotes interactions between the CNC-functionalized AFM tipless levers and cellulose/hemicellulose/lignin films. This observation is a consequence of the increased number and increased strength of the chemical bonds involved in the complex. Conditions of high RH enable the formation of hydrogen bonds.

We hope that our promising SMFS study can shed light on how lignocellulosic polymers interact among one another at the single molecule level. Our findings can provide a better understanding of the mechanism behind how these plant cell wall polymers interact with each other, which can elucidate the mechanism that governs the adhesion processes. The quantification and characterization of the intermolecular forces driven at nanoscale level represent a preliminary step towards promoting the design of new fully biosourced and performant composites using lignocellulosic polymers. Our measurements could lead to a better understanding of the interaction between different type of fibers (wood, hemp, flax…) and different polar or non-polar matrices. Such knowledge can be exploited by industries involved in food packaging, surface-based polymer-polymer interaction biosensors or the fabrication of novel nanocomposites made by these polymers with improved properties, such as tensile strength, endurance, permeability, and solubility, among others.

Acknowledgements

This work was funded by the Grand Est Region and the European FEDER Program [grant number D201550245] within COFILI project and a part of ANR INTOS2 [grant number ANR-18-CE93-0007]. The authors also thank the Nano'Mat platform funded by the Grand EST Region, the DDRT Grand Est and the European FEDER program.

Data availability

The raw/processed data required to reproduced these findings cannot be shared at this time as the data also forms part of an ongoing study.

Author information

To whom correspondence should be address at Institut National de la Recherche Agronomique (INRA) in Reims (France). Tel: +33 (0)326772579, email: carlos.marcuello-angles@inra.fr; michael.molinari@u-bordeaux.fr.

Author contributions

V.A.-B., B.C. and M.M conceived the project and decided on the scientific strategy. All authors conceived the methodology used, participated in the scientific discussions, and wrote the manuscript. C.M. carried out the experiments concerning the functionalization AFM tipless levers, AFM imaging, AFM force-distance curve acquisition, and nanomechanical AFM measurements and analyzed the raw data. L.F. isolated and characterized CNCs. V.A.-B and L.F. performed the LB technique and created cellulose/hemicellulose/lignin films. M.M designed and supervised AFM experiments. All the authors read and approved the final manuscript.

Abbreviations

AFM, atomic force microscopy; CNCs, cellulose nanocrystals; DMT, the Derjaguin, Muller and Toporov model; DLS, dynamic light scattering; DODA, dimethyldioctadecylammonium; eqn, equation; F, applied force; FTIR, Fourier transform infrared spectroscopy; GM, glucomannan, GPa, gigaPascal; h, hour; i, indentation step, JKR, the Johnson, Kendall and Roberts model; QCM, quartz crystal microbalance; RH, relative humidity; kHz, kilohertz; LB, Langmuir-Blodgett; LIG, lignin; N/m, Newton per meter; PF-QNM, Peak Force Quantitative Nanomechanics; OX-LIG, oxidized lignin; PFTE, polytetrafluoroethylene; R^*, reduced radius; RH, relative humidity; Rq, root mean square; SD, standard deviation; SiO_2, silicon dioxide; Si_3N_4, silicon nitride; ν, Poisson ratio; π, surface pressure.; XYL, xylan; YM, Young Modulus.

Competing Financial Interests

The authors declare no competing financial interests.

References

[1] A.K. Mohanty, S. Vivekanandhan, J.-M. Pin, M. Misra, Composites from renewable and sustainable resources: Challenges and innovations, Science 362(6414) (2018) 536-542. https://doi.org/10.1126/science.aat9072.

[2] H. Zhu, W. Luo, P.N. Ciesielski, Z. Fang, J.Y. Zhu, G. Henriksson, M.E. Himmel, L. Hu, Wood-Derived Materials for Green Electronics, Biological Devices, and Energy Applications, Chem. Rev. 116(16) (2016) 9305-9374. https://doi.org/10.1021/acs.chemrev.6b00225.

[3] F.H. Isikgor, C.R. Becer, Lignocellulosic biomass: a sustainable platform for the production of bio-based chemicals and polymers, Polym. Chem. 6(25) (2015) 4497-4559. https://doi.org/10.1039/C5PY00263J.

[4] E. Fortunati, W. Yang, F. Luzi, J. Kenny, L. Torre, D. Puglia, Lignocellulosic nanostructures as reinforcement in extruded and solvent casted polymeric nanocomposites: an overview, Eur. Polym. J. 80 (2016) 295-316. https://doi.org/10.1016/j.eurpolymj.2016.04.013.

[5] I. Šimkovic, Unexplored possibilities of all-polysaccharide composites, Carbohydr. Polym. 95(2) (2013) 697-715. https://doi.org/10.1016/j.carbpol.2013.03.040.

[6] N. Terashima, K. Kitano, M. Kojima, M. Yoshida, H. Yamamoto, U. Westermark, Nanostructural assembly of cellulose, hemicellulose, and lignin in the middle layer of secondary wall of ginkgo tracheid, J. Wood Sci. 55(6) (2009) 409-416. https://doi.org/10.1007/s10086-009-1049-x.

[7] A. Gallos, G. Paës, F. Allais, J. Beaugrand, Lignocellulosic fibers: a critical review of the extrusion process for enhancement of the properties of natural fiber composites, RSC Adv. 7(55) (2017) 34638-34654. https://doi.org/10.1039/C7RA05240E.

[8] R.J. Moon, A. Martini, J. Nairn, J. Simonsen, J. Youngblood, Cellulose nanomaterials review: structure, properties and nanocomposites, Chem. Soc. Rev. 40(7) (2011) 3941-3994. https://doi.org/10.1039/C0CS00108B.

[9] N.D. Wanasekara, S.J. Eichhorn, Injectable Highly Loaded Cellulose Nanocrystal Fibers and Composites, ACS Macro Lett. 6(10) (2017) 1066-1070. https://doi.org/10.1021/acsmacrolett.7b00609.

[10] E.J. Foster, R.J. Moon, U.P. Agarwal, M.J. Bortner, J. Bras, S. Camarero-Espinosa, K.J. Chan, M.J.D. Clift, E.D. Cranston, S.J. Eichhorn, D.M. Fox, W.Y. Hamad, L. Heux, B. Jean, M. Korey, W. Nieh, K.J. Ong, M.S. Reid, S. Renneckar, R. Roberts, J.A. Shatkin, J. Simonsen, K. Stinson-Bagby, N. Wanasekara, J. Youngblood, Current characterization methods for cellulose nanomaterials, Chem. Soc. Rev. 47(8) (2018) 2609-2679. https://doi.org/10.1039/C6CS00895J.

[11] V. Aguié-Beghin, G. Paës, M. Molinari, B. Chabbert, Films and coatings from lignocellulosic polymers, Edible Films and Coatings: Fundamentals and Applications, Pilar Montero M. 2017.

[12] M. Åkerholm, L. Salmén, Interactions between wood polymers studied by dynamic FT-IR spectroscopy, Polymer 42(3) (2001) 963-969. https://doi.org/10.1016/S0032-3861(00)00434-1.

[13] F. Picchioni, H. Muljana, Hydrogels Based on Dynamic Covalent and Non Covalent Bonds: A Chemistry Perspective, Gels 4(1) (2018) 21. https://doi.org/10.3390/gels4010021.

[14] E.D. Cranston, D.G. Gray, M.W. Rutland, Direct Surface Force Measurements of Polyelectrolyte Multilayer Films Containing Nanocrystalline Cellulose, Langmuir 26(22) (2010) 17190-17197. https://doi.org/10.1021/la1030729.

[15] A. Hambardzumyan, L. Foulon, B. Chabbert, V. Aguié-Béghin, Natural Organic UV-Absorbent Coatings Based on Cellulose and Lignin: Designed Effects on Spectroscopic Properties, Biomacromolecules 13(12) (2012) 4081-4088. https://doi.org/10.1021/bm301373b.
[16] D. Roy, M. Semsarilar, J.T. Guthrie, S. Perrier, Cellulose modification by polymer grafting: a review, Chem. Soc. Rev. 38(7) (2009) 2046-2064. https://doi.org/10.1039/B808639G.
[17] L. Muraille, M. Pernes, A. Habrant, R. Serimaa, M. Molinari, V. Aguié-Beghin, B. Chabbert, Impact of lignin on water sorption properties of bioinspired self-assemblies of lignocellulosic polymers, Eur. Polym. J. 64 (2015) 21–35. https://doi.org/10.1016/j.eurpolymj.2014.11.040.
[18] G. Fotie, R. Rampazzo, M.A. Ortenzi, S. Checchia, D. Fessas, L. Piergiovanni, The Effect of Moisture on Cellulose Nanocrystals Intended as a High Gas Barrier Coating on Flexible Packaging Materials, Polymers (Basel) 9(9) (2017) 415. https://doi.org/10.3390/polym9090415.
[19] F. Khan, N. Pilpel, S. Ingham, The effect of moisture on the density, compaction and tensile strength of microcrystalline cellulose, Powder Technol. 54(3) (1988) 161-164. https://doi.org/10.1016/0032-5910(88)80074-3.
[20] K. Kulasinski, L. Salmén, D. Derome, J. Carmeliet, Moisture adsorption of glucomannan and xylan hemicelluloses, Cellulose 23(3) (2016) 1629-1637. https://doi.org/10.1007/s10570-016-0944-8.
[21] A. Gupta, G.E. Peck, R.W. Miller, K.R. Morris, Influence of ambient moisture on the compaction behavior of microcrystalline cellulose powder undergoing uni-axial compression and roller-compaction: A comparative study using near-infrared spectroscopy, J. Pharm. Sci. 94(10) (2005) 2301-2313. https://doi.org/10.1002/jps.20430.
[22] W.J. Cousins, Young's modulus of hemicellulose as related to moisture content, Wood Sci. Technol. 12(3) (1978) 161-167. https://doi.org/10.1007/BF00372862.
[23] A. Kaya, D. A. Drazenovich, W. Glasser, T. Heinze, A. Esker, Hydroxypropyl Xylan Self-Assembly at Air/Water and Water/Cellulose Interfaces, Model Cellulosic Surfaces, ACS Symp. Ser. 2010, pp. 173-191. https://doi.org/10.1021/bk-2009-1019.ch008.
[24] P. Eronen, M. Österberg, S. Heikkinen, M. Tenkanen, J. Laine, Interactions of structurally different hemicelluloses with nanofibrillar cellulose, Carbohydr. Polym. 86(3) (2011) 1281-1290. https://doi.org/10.1016/j.carbpol.2011.06.031.
[25] M. Rief, H. Grubmüller, Force Spectroscopy of Single Biomolecules, ChemPhysChem 3(3) (2002) 255-261. https://doi.org/10.1002/1439-7641(20020315)3:3<255::AID-CPHC255>3.0.CO;2-M.
[26] R.R. Lahiji, X. Xu, R. Reifenberger, A. Raman, A. Rudie, R.J. Moon, Atomic Force Microscopy Characterization of Cellulose Nanocrystals, Langmuir 26(6) (2010) 4480-4488. https://doi.org/10.1021/la903111j.
[27] S. Heikkinen, K. Mikkonen, P. Koivisto, M. I. Heikkilä, K. Pirkkalainen, V. Liljeström, R. Serimaa, M. Tenkanen, Long-Term Physical Stability of Plasticized Hemicellulose Films, BioResources 9(1) (2014) 906-921. https://doi.org/10.15376/biores.9.1.906-921.
[28] L. Muraille, V. Aguié-Béghin, B. Chabbert, M. Molinari, Bioinspired lignocellulosic films to understand the mechanical properties of lignified plant cell walls at nanoscale, Sci. Rep. 7 (2017) 44065. https://doi.org/10.1038/srep44065.

[29] F. Khelifa, Y. Habibi, P. Leclère, P. Dubois, Convection-assisted assembly of cellulose nanowhiskers embedded in an acrylic copolymer, Nanoscale 5 (3) (2013) 1082-1090. https://doi.org/10.1039/C2NR33194B.
[30] S. Xu, M. Dong, X. Liu, K.A. Howard, J. Kjems, F. Besenbacher, Direct force measurements between siRNA and chitosan molecules using force spectroscopy, Biophys. J. 93(3) (2007) 952-959.
https://doi.org/10.1529/biophysj.106.093229
[31] P. Lazar, S, Zhang, K. Šafářová, Q. Li, J.P. Froning, J. Granatier, P. Hobza, R. Zbořil, F. Besenbacher, M. Dong, M. Otyepka, Quantification of the Interaction Forces between Metals and Graphene by Quantum Chemical Calculations and Dynamic Force Measurements under Ambient Conditions, ACS Nano 7(2) (2013) 1646-1651. https://doi.org/10.1021/nn305608a.
[32] K.C. Neuman, A. Nagy, Single-molecule force spectroscopy: optical tweezers, magnetic tweezers and atomic force microscopy, Nat. Methods 5 (2008) 491. https://doi.org/10.1038/nmeth.1218.
[33] F. Kienberger, C. Rankl, V. Pastushenko, R. Zhu, D. Blaas, P. Hinterdorfer, Visualization of Single Receptor Molecules Bound to Human Rhinovirus under Physiological Conditions, Structure 13(9) (2005) 1247-1253. https://doi.org/10.1016/j.str.2005.06.012.
[34] C. Marcuello, L. Foulon, B. Chabbert, M. Molinari, V. Aguié-Béghin, Langmuir–Blodgett Procedure to Precisely Control the Coverage of Functionalized AFM Cantilevers for SMFS Measurements: Application with Cellulose Nanocrystals, Langmuir 34(32) (2018) 9376-9386. https://doi.org/10.1021/acs.langmuir.8b01892.
[35] V. Aguié-Béghin, M. Molinari. A. Hambardzumyan, L. Foulon, Y. Habibi, T. Heim, R. Blossey, R. Douillard. Preparation of ordered films of Cellulose nanocrystala in Model cellulosic surfaces. Ed. M. Roman, ACS Division of Cellulose and renewable materials 2009, pp. 115-136. https://doi.org/10.1021/bk-2009-1019.
[36] B. Monties, Preparation of dioxane lignin fractions by acidolysis, Methods in Enzymology, Academic Press 1988, pp. 31-35. https://doi.org/10.1016/0076-6879(88)61006-8.
[37] A. Hambardzumyan, L. Foulon, N.B. Bercu, M. Pernes, J.E. Maigret, M. Molinari, B. Chabbert, V. Aguié-Béghin, Organosolv lignin as natural grafting additive to improve the water resistance of films using cellulose nanocrystals, Chem. Eng. J. 264 (2015) 780-788. https://doi.org/10.1016/j.cej.2014.12.004.
[38] H.G. Hansma, R.L. Sinsheimer, J. Groppe, T.C. Bruice, V. Elings, G. Gurley, M. Bezanilla, I.A. Mastrangelo, P.V.C. Hough, P.K. Hansma, Recent advances in atomic force microscopy of DNA, Scanning 15(5) (1993) 296-299.
https://doi.org/10.1002/sca.4950150509.
[39] M. Encinar, S. Casado, A. Calzado-Martín, P. Natale, Á. San Paulo, M. Calleja, M. Vélez, F. Monroy, I. López-Montero, Nanomechanical properties of composite protein networks of erythroid membranes at lipid surfaces, Colloid Surface B 149 (2017) 174-183. https://doi.org/10.1016/j.colsurfb.2016.10.022.
[40] F. Akhatova, G. Fakhrullina, E. Khakimova, R. Fakhrullin, Atomic force microscopy for imaging and nanomechanical characterisation of live nematode epicuticle: A comparative Caenorhabditis elegans and Turbatrix aceti study, Ultramicroscopy 194 (2018) 40-47. https://doi.org/10.1016/j.ultramic.2018.07.008.
[41] J. Mandal, R.S. Varunprasaath, W. Yan, M. Divandari, N.D. Spencer, M. Dübner, In situ monitoring of SI-ATRP throughout multiple reinitiations under flow by means of

a quartz crystal microbalance, RSC Adv 8(36) (2018) 20048-20055. https://doi.org/10.1039/C8RA03073A.
[42] D. Nečas, P. Klapetek, Gwyddion: an open-source software for SPM data analysis, Central Eur. J. Phys. 10(1) (2012) 181-188. https://doi.org/10.2478/s11534-011-0096-2.
[43] J.E. Sader, J.W.M. Chon, P. Mulvaney, Calibration of rectangular atomic force microscope cantilevers, Rev. Sci. Instrum. 70(10) (1999) 3967-3969. https://doi.org/10.1063/1.1150021.
[44] D. Tranchida, S. Piccarolo, R.A.C. Deblieck, Some experimental issues of AFM tip blind estimation: the effect of noise and resolution, Meas. Sci. Technol. 17(10) (2006) 2630. https://doi.org/10.1088/0957-0233/17/10/014.
[45] H. Hertz, Ueber die Berührung fester elastischer Körper, J. Reine Angew. Math. 92 (1882). https://doi.org/10.1515/crll.1882.92.156.
[46] K.L. Johnson, K. Kendall, A.D. and Roberts, Surface Energy and Contact of Elastic Solids, P. Roy. Soc. A-Math. Phy. 324(1558) (1971) 301-313. https://doi.org/10.1098/rspa.1971.0141.
[47] B.V. Derjaguin, V.M. Muller, Y.P. Toporov, Effect of contact deformations on the adhesion of particles, J. Colloid Interface Sci. 53(2) (1975) 314-326. https://doi.org/10.1016/0021-9797(75)90018-1.
[48] E. Chanliaud, K.M. Burrows, G. Jeronimidis, M.J. Gidley, Mechanical properties of primary plant cell wall analogues, Planta 215(6) (2002) 989-996. https://doi.org/10.1007/s00425-002-0783-8.
[49] I.D. Cave, The anisotropic elasticity of the plant cell wall, Wood Sci. Technol. 2(4) (1968) 268-278. https://doi.org/10.1007/BF00350273.
[50] H.Y. She, B.E. Sleep, The effect of temperature on capillary pressure-saturation relationships for air-water and perchloroethylene-water systems, Water Resour. Res. 34(10) (1998) 2587-2597. https://doi.org/10.1029/98WR01199.
[51] L.A. Richards, Capillary conduction of liquids in porous mediums. Physics, 1 (1931) 318-333. https://doi.org/10.1063/1.1745010.
[52] H.D. Chanzy, A. Grosrenaud, J.P. Joseleau, M. Dubé, R.H. Marchessault, Crystallization behavior of glucomannan, Biopolymers 21(2) (1982) 301-319. https://doi.org/10.1002/bip.360210206.
[53] A. Pereira, I.C. Hoeger, A. Ferrer, J. Rencoret, J.C. del Rio, K. Kruus, J. Rahikainen, M. Kellock, A. Gutiérrez, O.J. Rojas, Lignin Films from Spruce, Eucalyptus, and Wheat Straw Studied with Electroacoustic and Optical Sensors: Effect of Composition and Electrostatic Screening on Enzyme Binding, Biomacromolecules 18(4) (2017) 1322-1332. https://doi.org/10.1021/acs.biomac.7b00071.
[54] K. Mazeau, A. Rivet, Wetting the (110) and (100) Surfaces of Iβ Cellulose Studied by Molecular Dynamics, Biomacromolecules 9(4) (2008) 1352-1354. https://doi.org/10.1021/bm7013872.
[55] A. Bergander, L. Salmén, Cell wall properties and their effects on the mechanical properties of fibers, J. Mater. Sci. 37(1) (2002) 151-156. https://doi.org/10.1023/A:1013115925679.
[56] S. Youssefian, N. Rahbar, Molecular Origin of Strength and Stiffness in Bamboo Fibrils, Sci. Rep. 5 (2015) 11116. https://doi.org/10.1038/srep11116.
[57] K.M. Hess, J. Killgore, W. Srubar Iii, Nanoscale hygromechanical behavior of lignin, Cellulose 25(11) 2018 6345-6360. https://doi.org/10.1007/s10570-018-2045-3.

[58] S.P.S. Rawat, D.P. Khali, Studies on adsorption behaviour of water vapour in lignin using the Brunauer-Emmett-Teller theory, Holz Roh Werkst. 57(3) (1999) 203-204. https://doi.org/10.1007/s001070050040.
[59] N. Volkova, V. Ibrahim, R. Hatti-Kaul, L. Wadsö, Water sorption isotherms of Kraft lignin and its composites, Carbohydr. Polym. 87(2) (2012) 1817-1821. https://doi.org/10.1016/j.carbpol.2011.10.001.
[60] G. Elegir, D. Bussini, S. Antonsson, M.E. Lindström, L. Zoia, Laccase-initiated cross-linking of lignocellulose fibres using a ultra-filtered lignin isolated from kraft black liquor, Appl. Microbiol. Biotechnol. 77(4) (2007) 809-817. https://doi.org/10.1007/s00253-007-1203-6.
[61] M.-L. Mattinen, J.J. Valle-Delgado, T. Leskinen, T. Anttila, G. Riviere, M. Sipponen, A. Paananen, K. Lintinen, M. Kostiainen, M. Österberg, Enzymatically and chemically oxidized lignin nanoparticles for biomaterial applications, Enzyme Microb. Tech. 111 (2018) 48-56. https://doi.org/10.1016/j.enzmictec.2018.01.005.
[62] J.N. Israelachvili, 17 - Adhesion and Wetting Phenomena, Intermolecular and Surface Forces (Third Edition), Academic Press, San Diego, 2011, pp. 415-467. https://doi.org/10.1016/C2009-0-21560-1.
[63] D.L. Sedin, K.L. Rowlen, Adhesion Forces Measured by Atomic Force Microscopy in Humid Air, Anal. Chem. 72(10) (2000) 2183-2189. https://doi.org/10.1021/ac991198c.
[64] K. Hofstetter, B. Hinterstoisser, L. Salmén, Moisture uptake in native cellulose – the roles of different hydrogen bonds: a dynamic FT-IR study using Deuterium exchange, Cellulose 13(2) (2006) 131-145. https://doi.org/10.1007/s10570-006-9055-2.
[65] X. Jin, B. Kasal, Adhesion force mapping on wood by atomic force microscopy: influence of surface roughness and tip geometry, R Soc Open Sci 3(10) (2016) 160248-160248. https://doi.org/10.1098/rsos.160248.
[66] Z. Yu, Y. Jiang, W. Zou, J. Duan, X. Xiong, Preparation and characterization of cellulose and konjac glucomannan blend film from ionic liquid, J. Polym. Sci. Pol. Phys. 47(17) (2009) 1686-1694. https://doi.org/10.1002/polb.21768.
[67] C. Xiao, Y. Lu, H. Liu, L. Zhang, Preparation and characterization of konjac glucomannan and sodium carboxymethylcellulose blend films, J. Appl. Polym. Sci. 80(1) (2001) 26-31.
https://doi.org/10.1002/1097-4628(20010404)80:1<26::AID-APP1070>3.0.CO;2-B.
[68] L.P. Christopher, B. Yao, Y. Ji, Lignin Biodegradation with Laccase-Mediator Systems, Front. Energy Res. 2(12) (2014). https://doi.org/10.3389/fenrg.2014.00012.
[69] M.S. Kent, I.C. Avina, N. Rader, M.L. Busse, A. George, N. Sathitsuksanoh, E. Baidoo, J. Timlin, N.H. Giron, M.C. Celina, L.E. Martin, R. Polsky, V.H. Chavez, D.L. Huber, J.D. Keasling, S. Singh, B.A. Simmons, K.L. Sale, Assay for lignin breakdown based on lignin films: insights into the Fenton reaction with insoluble lignin, Green Chem. 17(10) (2015) 4830-4845. https://doi.org/10.1039/C5GC01083G.
[70] Y. Nishiyama, P. Langan, H. Chanzy, Crystal Structure and Hydrogen-Bonding System in Cellulose Iβ from Synchrotron X-ray and Neutron Fiber Diffraction, J. Am. Chem. Soc. 124(31) (2002) 9074-9082. https://doi.org/10.1021/ja0257319.
[71] M. Österberg, On the interactions in cellulose systems: surface forces and adsorption, Trita-YTK, Kemi, Stockholm, 2000.
[72] V. Aguié-Béghin, L. Foulon, P. Soto, D. Crônier, E. Corti, F. Legée, L. Cézard, B. Chabbert, M.-N. Maillard, W.J.J. Huijgen, S. Baumberger, Use of Food and Packaging

Model Matrices to Investigate the Antioxidant Properties of Biorefinery Grass Lignins, J. Agric. Food Chem. 63(45) (2015) 10022-10031. https://doi.org/10.1021/acs.jafc.5b03686.

Tables

	Rq (nm) at RH = 15 %	Rq (nm) at RH = 45 %	Rq (nm) at RH = 65 %	Rq (nm) at RH = 95 %
CNCs	6.2 ± 0.2	6.2 ± 0.2	6.3 ± 0.3	6.4 ± 0.2
GM	8.9 ± 0.5	9.1 ± 0.7	9.2 ± 0.5	9.4 ± 0.6
XYL	23.5 ± 1.5	23.6 ± 1.8	23.5 ± 1.4	23.5 ± 1.4
LIG	10.0 ± 0.4	10.0 ± 0.5	10.1 ± 0.4	10.1 ± 0.5
OX-LIG	20.1 ± 1.8	20.1 ± 1.7	20.2 ± 1.7	20.2 ± 1.9

Table 1. Evolution of the Rq roughness parameter with RH.

π (mN/m)	RH (%)	CNCs:CNCs (nN)	CNCs:GM (nN)	CNCs:XYL (nN)	CNCs:LIG (nN)	CNCs:OX-LIG (nN)
------	15.0	75.8 ± 24.1	------	------	------	------
------	45.0	86.6 ± 25.5	------	------	------	------
------	65.0	91.0 ± 23.9	------	------	------	------
------	95.0	96.7 ± 26.3	------	------	------	------
5	15.0	4.3 ± 0.4	6.4 ± 0.4	3.1 ± 0.2	8.2 ± 0.5	5.2 ± 0.7
5	45.0	4.6 ± 0.6	6.7 ± 0.4	3.4 ± 0.3	8.6 ± 0.5	5.4 ± 0.7
5	65.0	4.9 ± 0.5	6.8 ± 0.3	4.2 ± 0.5	8.7 ± 0.6	5.9 ± 0.8
5	95.0	5.1 ± 0.6	6.8 ± 0.3	4.3 ± 0.6	8.9 ± 0.6	6.1 ± 0.8
5	15.0	4.3 ± 0.4	6.4 ± 0.4	3.1 ± 0.2	8.2 ± 0.5	5.2 ± 0.7
15	45.0	8.3 ± 0.5	25.7 ± 2.6	8.8 ± 4.8	24.9 ± 8.4	8.4 ± 2.2
15	65.0	8.1 ± 0.4	32.9 ± 3.1	10.0 ± 4.4	27.0 ± 8.3	10.4 ± 2.0
15	95.0	13.7 ± 1.7	32.1 ± 3.1	10.8 ± 4.5	28.8 ± 8.2	13.7 ± 2.0
30	15.0	14.7 ± 1.0	37.5 ± 4.5	8.8 ± 1.5	43.6 ± 17.1	15.8 ± 4.9
30	45.0	14.7 ± 3.0	42.6 ± 4.1	11.4 ± 2.5	48.0 ± 17.5	16.8 ± 4.8
30	65.0	16.1 ± 1.5	47.9 ± 5.7	11.5 ± 3.5	47.4 ± 18.0	17.4 ± 5.0
30	95.0	16.7 ± 2.1	51.7 ± 4.7	11.8 ± 2.8	54.0 ± 18.2	17.1 ± 5.4

Table 2. Comparison of adhesion forces between AFM levers with functionalized CNCs by LB at values of π of 5, 15 and 30 mN/m and the CNC, XYL, GM, LIG and OX-LIG films at different values of RH.

Figure captions

Figure 1. Representative AFM topography images for cellulose/hemicellulose/lignin films: (A) cellulose nanocrystals, (B) glucomannan, (C) xylan, and (D) lignin before and (E) after laccase enzyme-mediated oxidation films at 45 % RH. The scan size for all images is 25 μm^2. The inset figures represent magnifications of the studied cellulose/hemicellulose/lignin films. The scan sizes and scale bars for all insets are 1 μm^2 and 200 nm, respectively. (F) The root mean square (Rq) roughness parameters for all cellulose/hemicellulose/lignin films is at 45 % RH. (G) and (H) Crossection profiles from LIG and OX-LIG AFM images, respectively.

Figure 2. Reduced Young modulus mapping at different RHs for CNC, GM, XYL, LIG and OX-LIG films (from the first to the fifth row). DMT channels (Size: 5 µm x 5 µm) are at RHs of 15 %, 45 % and 95 % are indicated going from the first to the third column. The inset figures depict magnifications of the studied cellulose/hemicellulose/lignin DMT maps. The scale bars for all insets are 200 nm.

Figure 3. Changes in the reduced YM of cellulose/hemicellulose/lignin films with respect to RH. Numbers 1, 2, 3, and 4 correspond to 15, 45, 65, and 95 % RH, respectively. Mean values of Young's modulus are significantly different concerning the RH (student's t test statistically analysis, $p<0.05$).

Figure 4. Force volume experiments with a CNC-functionalized AFM lever by LB at π = 15 mN/m. The topography channel and adhesion force map concerning CNC, GM, XYL, LIG and OX-LIG films. The scan size is 4 μm^2 for the CNC casting film and 25 μm^2 for hemicellulose/lignin films. RH is fixed at 45 ± 0.3 %.

Figure 5. Adhesion forces versus relative humidity for CNC-functionalized AFM levers obtained by LB at a π of 5, 15 and 30 mN/m with CNCs, GM, XYL, LIG and OX-LIG. The information related to the error bars of the adhesion force measurements appears on Table 2.

Figure 6. Correlation of the adhesion forces on the CNC-functionalized AFM lever at a π of 30 mN/m and the reduced YM of LIG and OX-LIG films at different RHs.

Supplementary information (SI) captions

Figure SI 1. AFM image of the functionalized CNC-lever by LB procedure at π of 15 mN/m (CNCs coverage of 32.8 ± 6.9 %).

Figure SI 2. YM properties of the OX-LIG film. (A) Topography map. (B) DMT channel. The scan size is 4 μm^2, and RH is fixed at 45 ± 0.3 %.

Figure SI 3. Histograms of the reduced Young's modulus of LIG films for all tested RH values.

Figure SI 4. Representative force-distance curves for unmodified AFM lever with CNCs film and CNC-functionalized AFM levers at a π of 15 mN/m and CNCs, GM, XYL, LIG and OX-LIG. RH = 45 %.

Figure SI 5. Force distribution of CNC-functionalized levers at π of 15 mN/m with CNCs films at RH of 15 %, 45 %, 65 % and 95 %.

Figure SI 6. Force volume experiments with unmodified AFM lever (negative control). The topography channel and adhesion force map concerning CNC, GM, XYL, LIG and OX-LIG films. The scan size is 4 μm^2 for the CNC casting film and 25 μm^2 for hemicellulose/lignin films. RH is fixed at 45 ± 0.3 %.

Figure SI 7. Force distribution of unmodified AFM levers with CNCs and LIG films at RH of 15 %, 45 %, 65 % and 95 %.

Figure SI 8. Correlation of the adhesion forces on CNC-functionalized AFM levers at π of 5, 15 and 30 mN/m with the reduced YM of the cellulose/hemicellulose/lignin films.

Figures

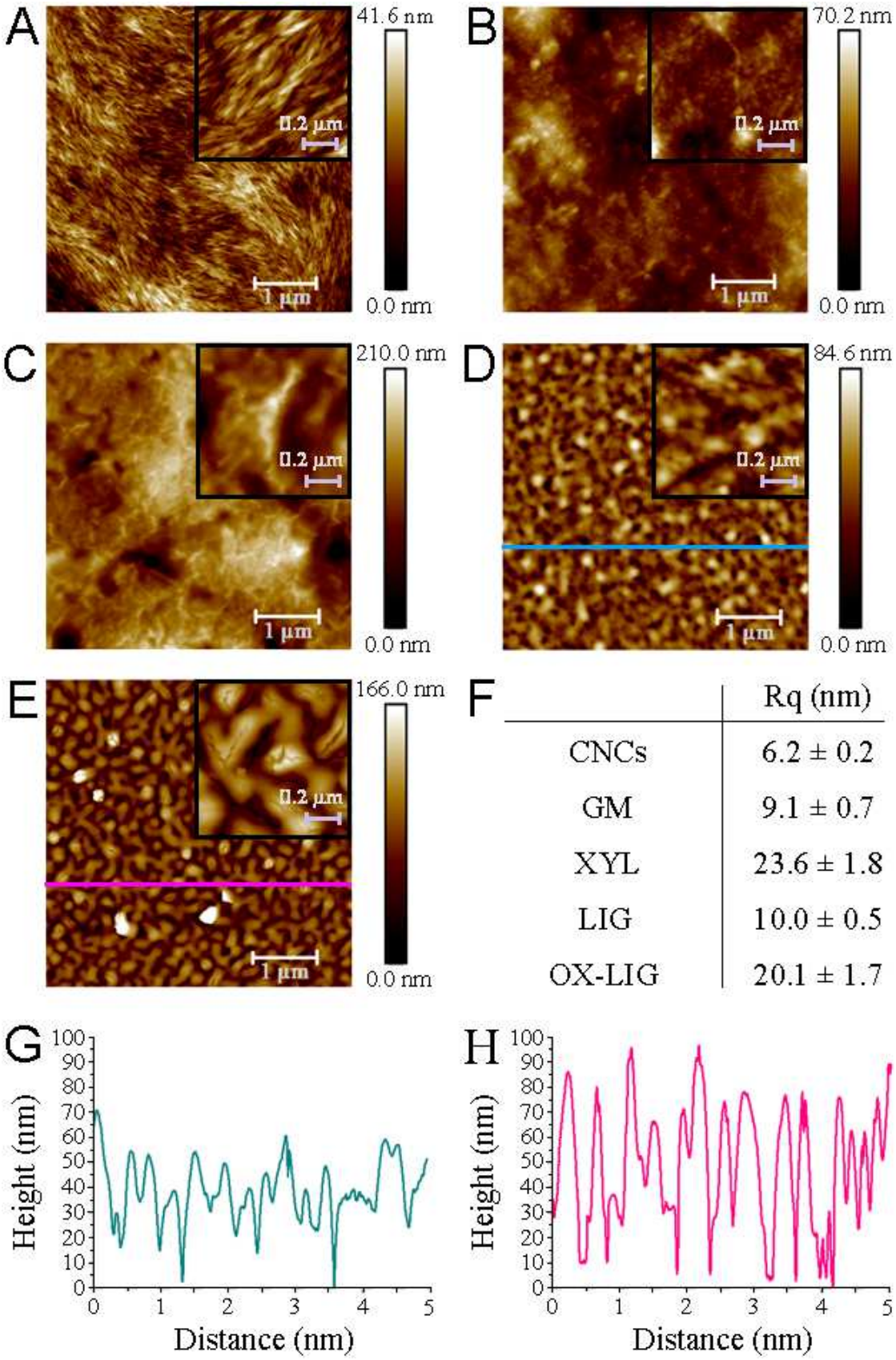

Int. J. Biol. Macromol. Carlos Marcuello and Michael Molinari. Fig. 1

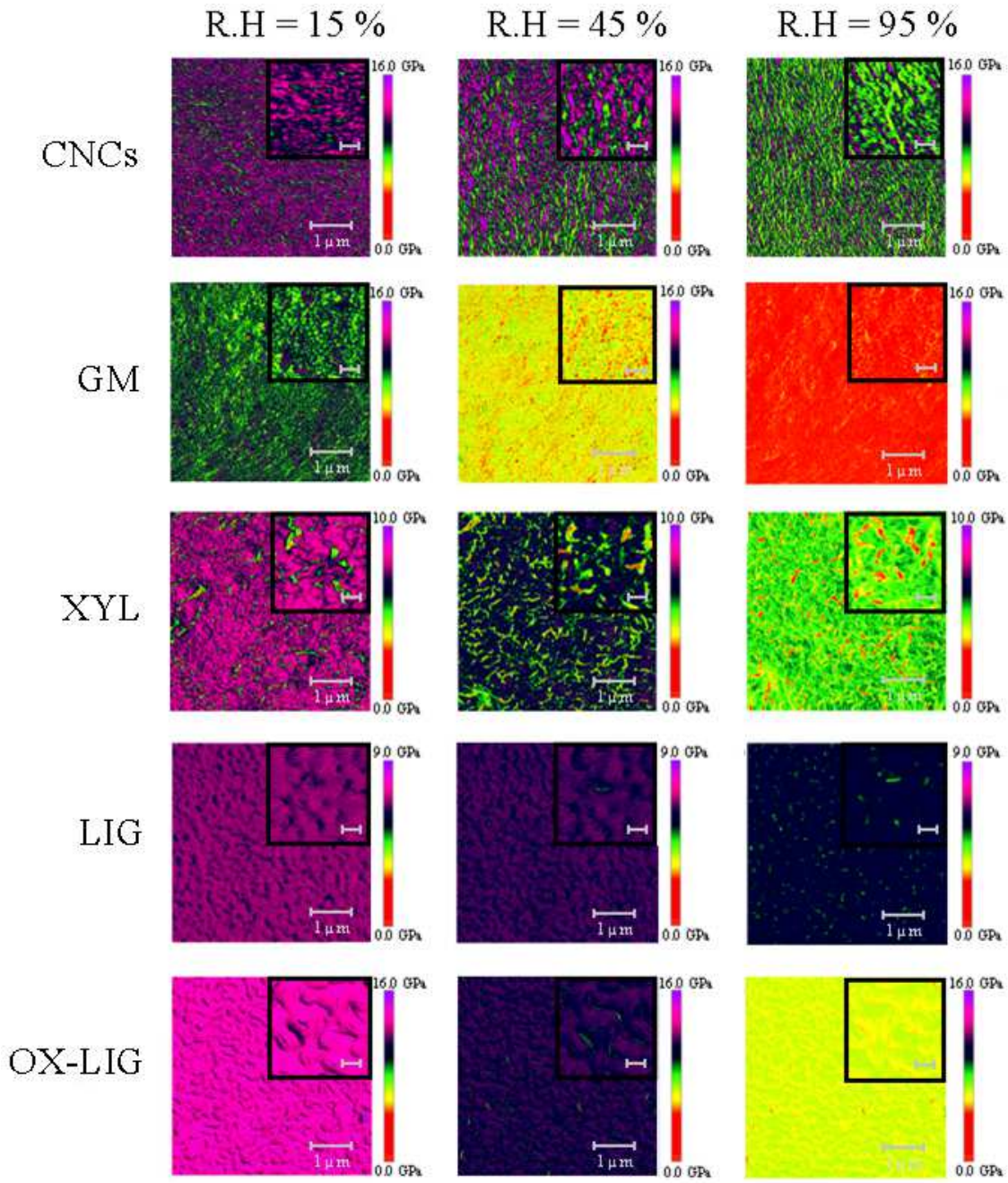

Int. J. Biol. Macromol. Carlos Marcuello and Michael Molinari. Fig. 2

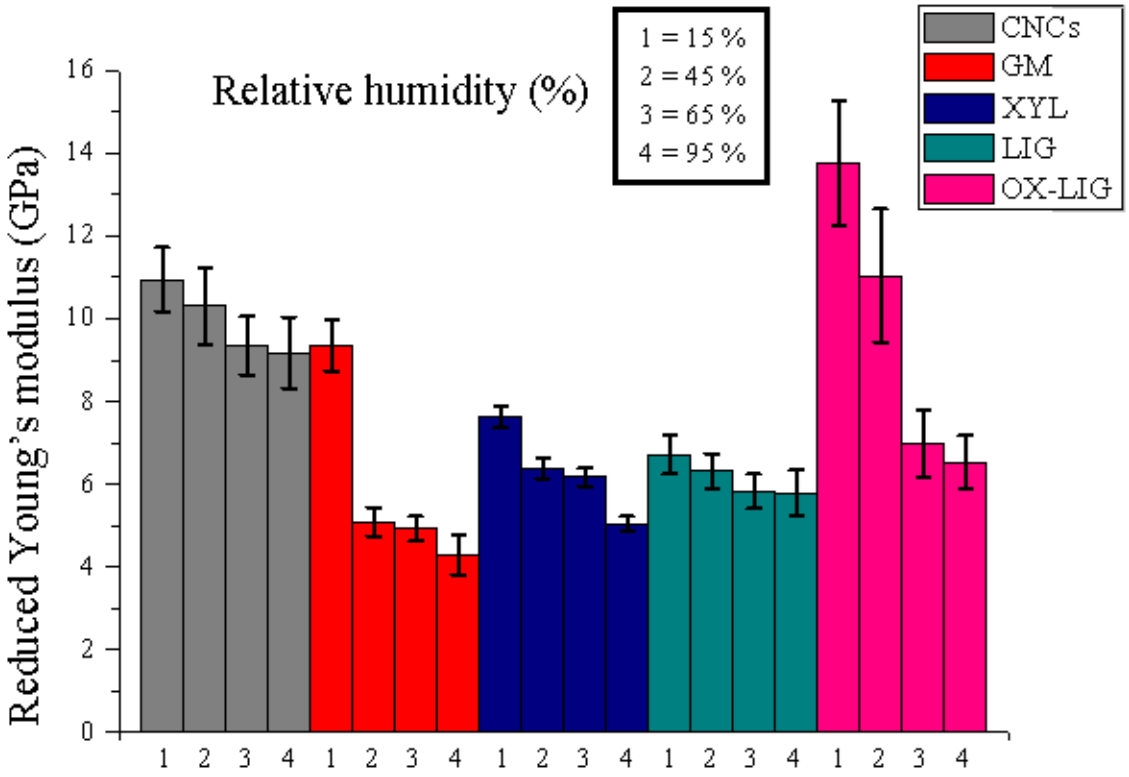

Int. J. Biol. Macromol. Carlos Marcuello and Michael Molinari. Fig. 3

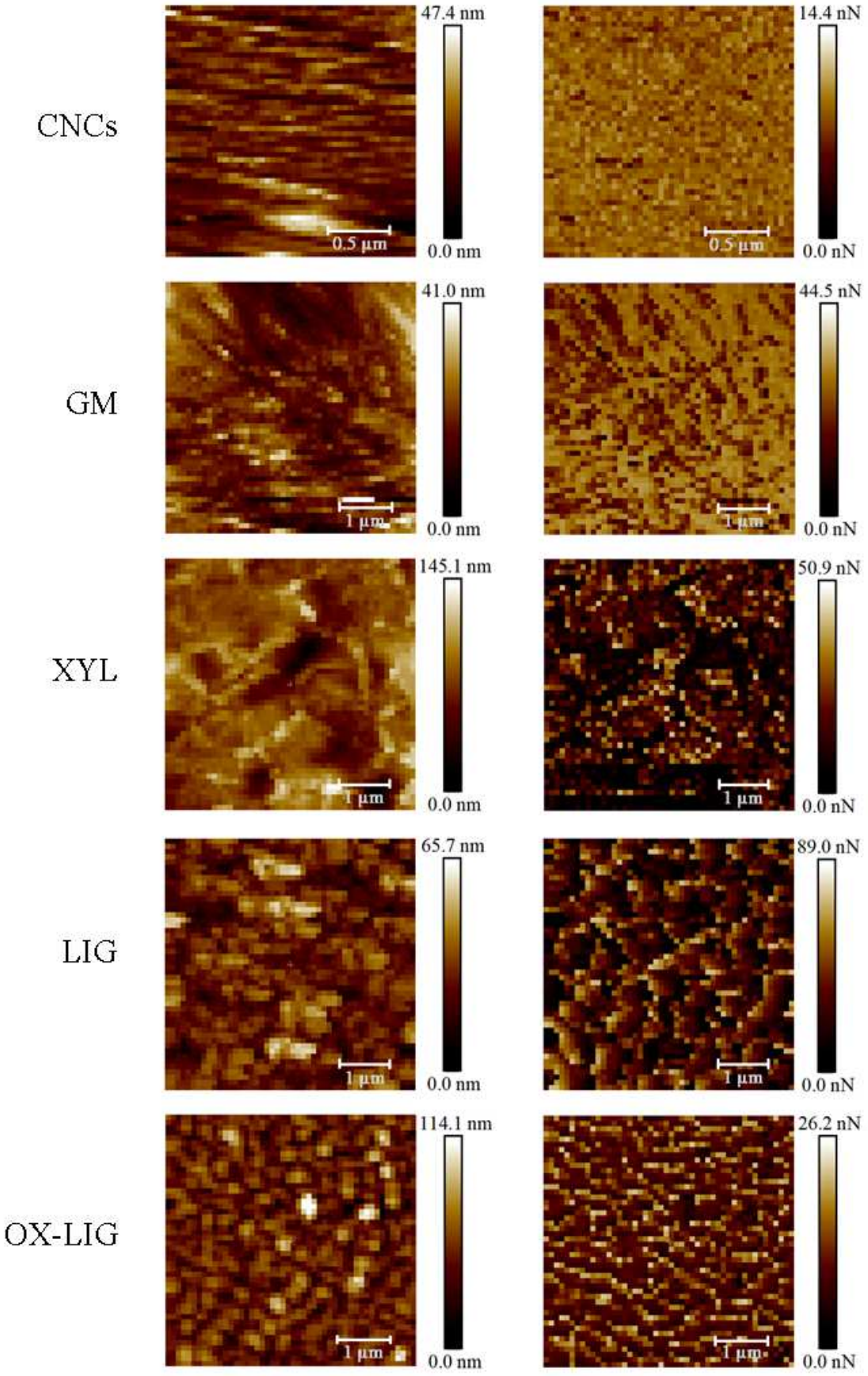

Int. J. Biol. Macromol. Carlos Marcuello and Michael Molinari. Fig. 4

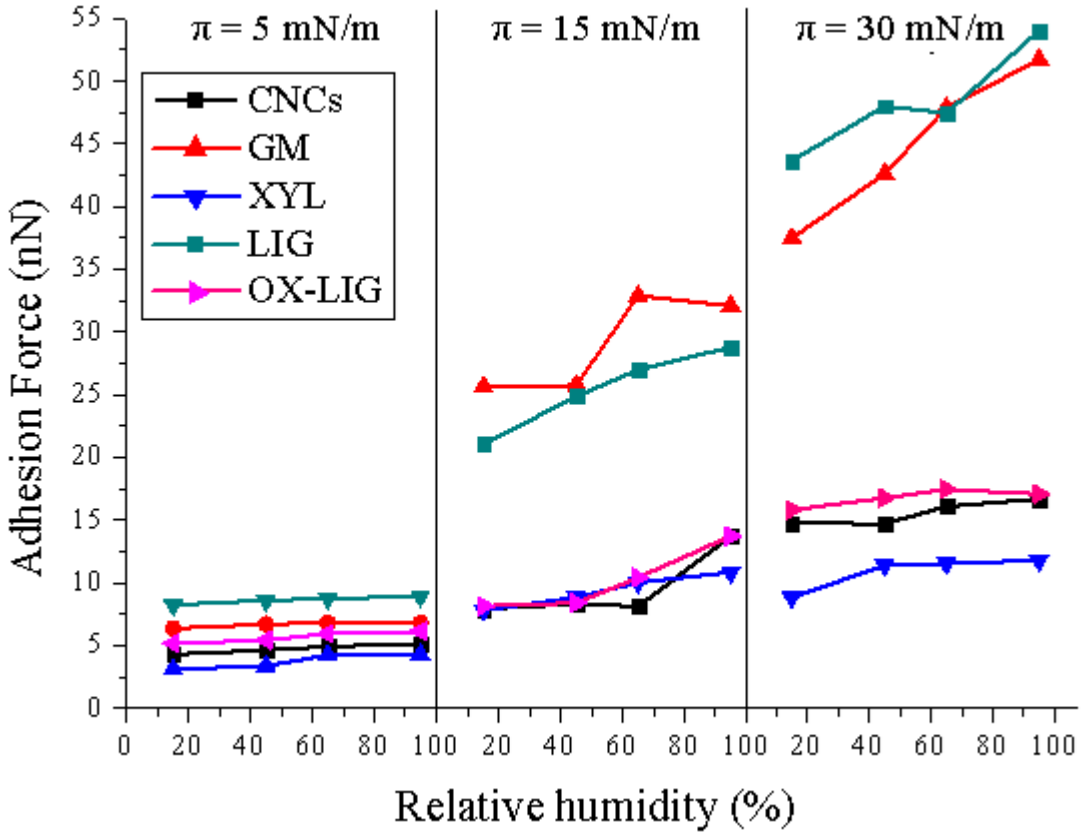

Int. J. Biol. Macromol. Carlos Marcuello and Michael Molinari. Fig. 5

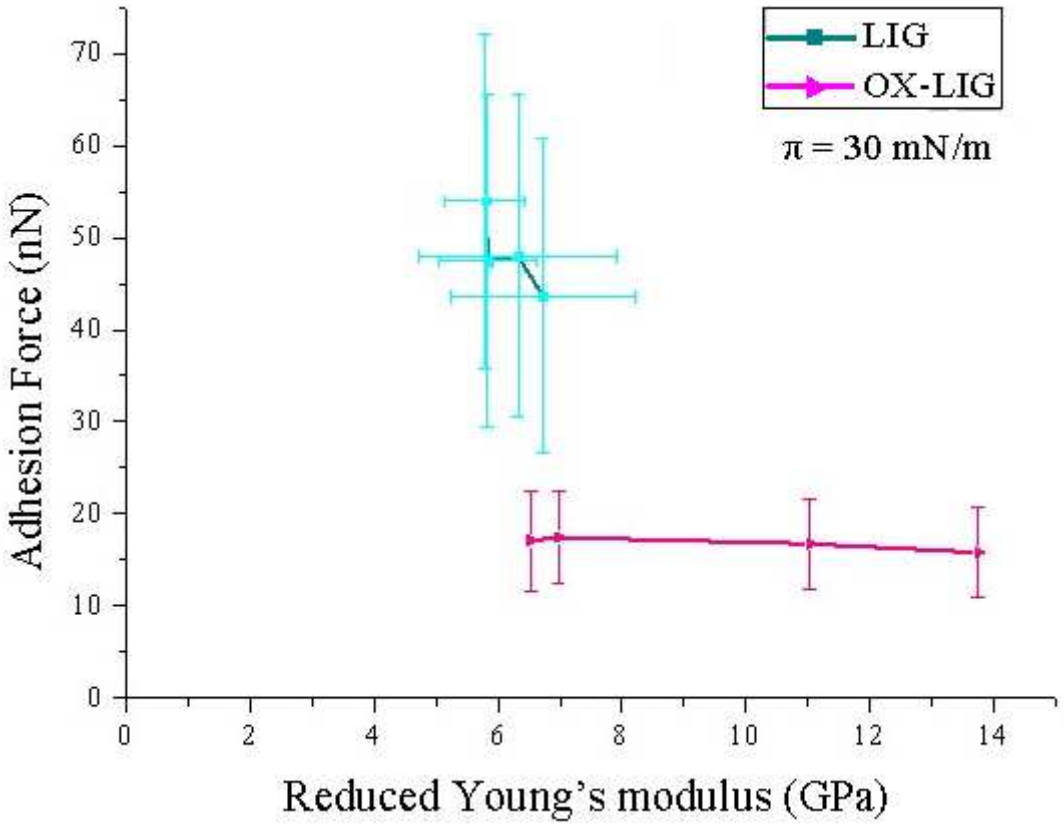

Int. J. Biol. Macromol. Carlos Marcuello and Michael Molinari. Fig. 6

Supplementary information (SI)

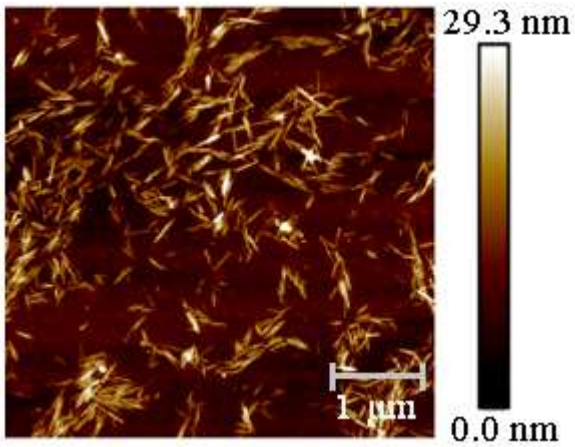

Int. J. Biol. Macromol. Carlos Marcuello and Michael Molinari. Fig. SI 1

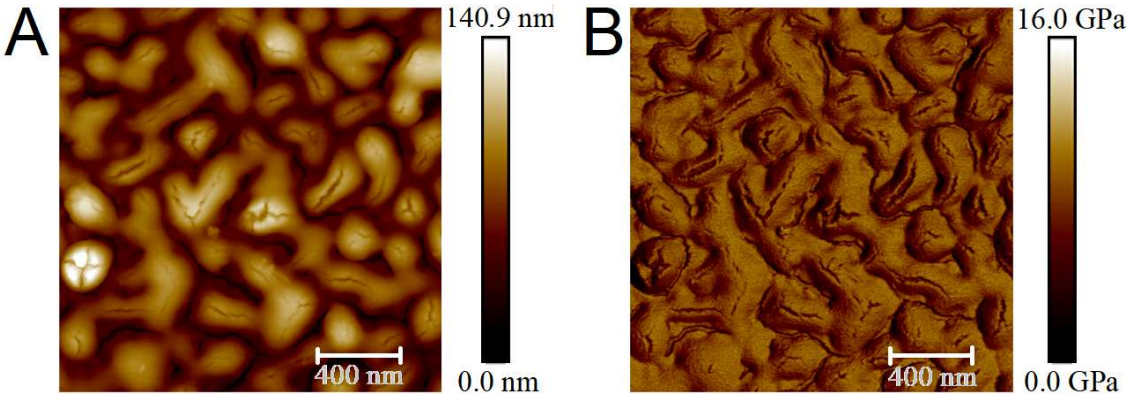

Int. J. Biol. Macromol. Carlos Marcuello and Michael Molinari. Fig. SI 2

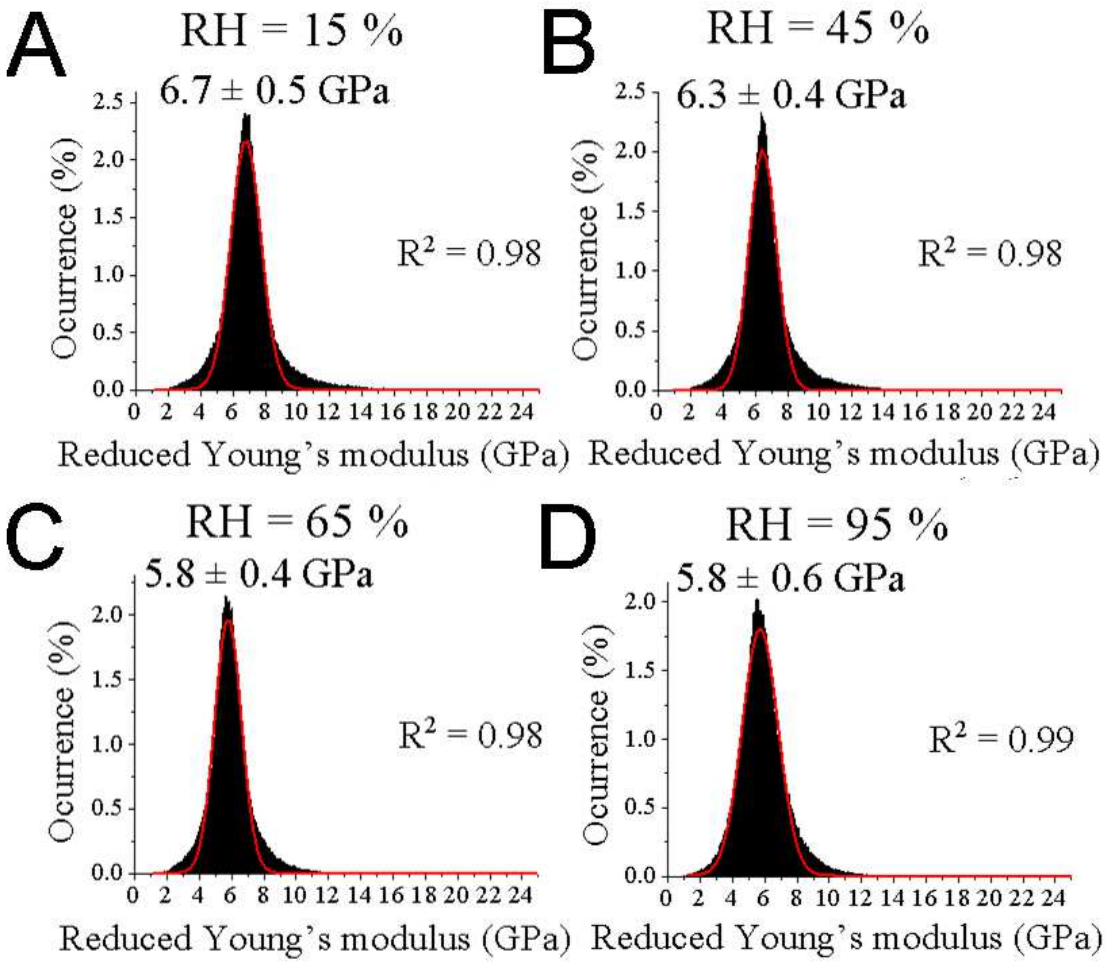

Int. J. Biol. Macromol. Carlos Marcuello and Michael Molinari. Fig. SI 3

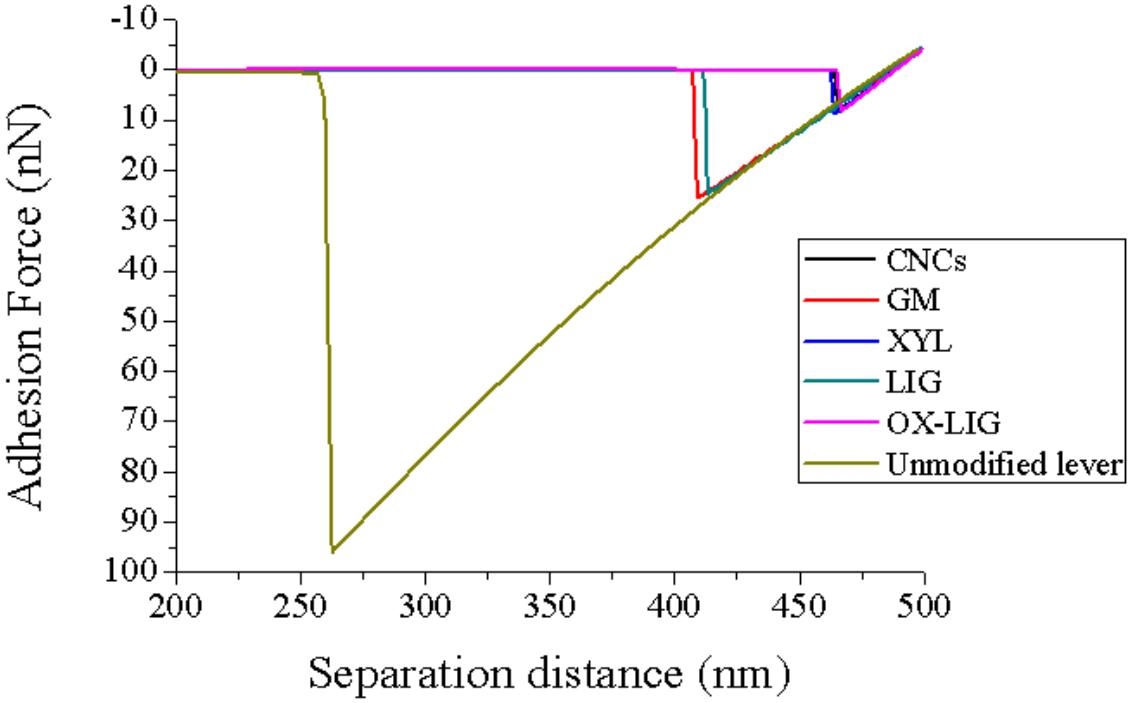

Int. J. Biol. Macromol. Carlos Marcuello and Michael Molinari. Fig. SI 4

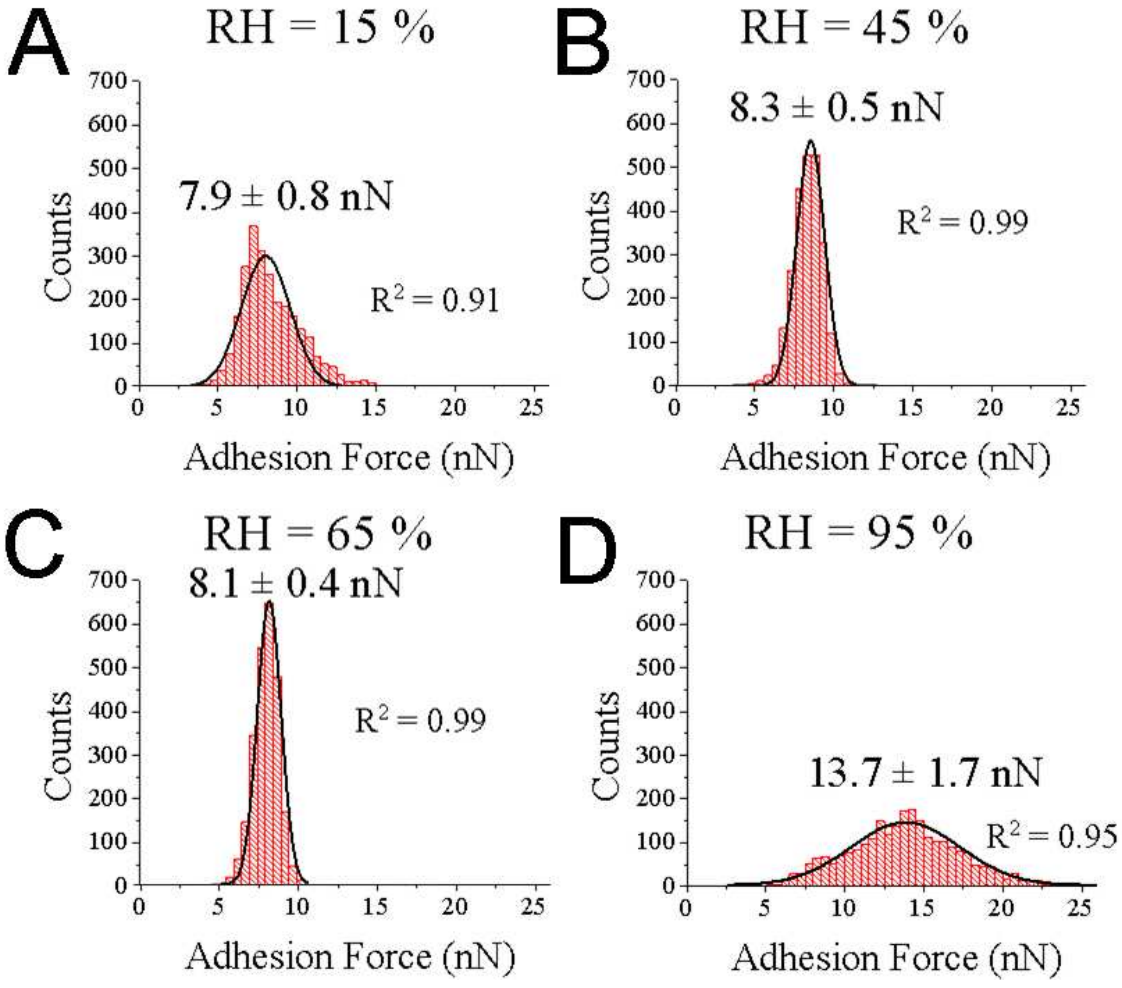

Int. J. Biol. Macromol. Carlos Marcuello and Michael Molinari. Fig. SI 5

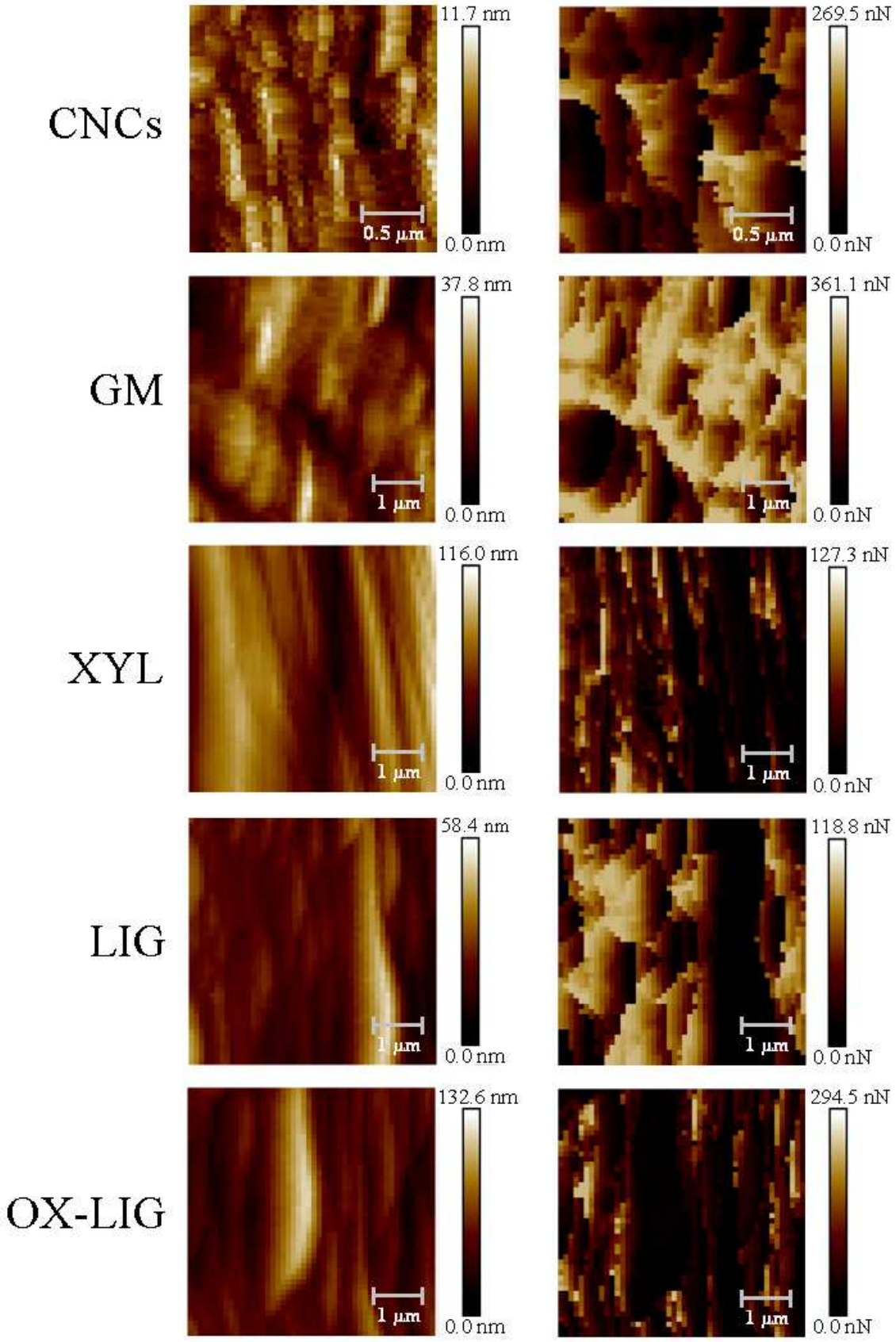

Int. J. Biol. Macromol. Carlos Marcuello and Michael Molinari. Fig. SI 6

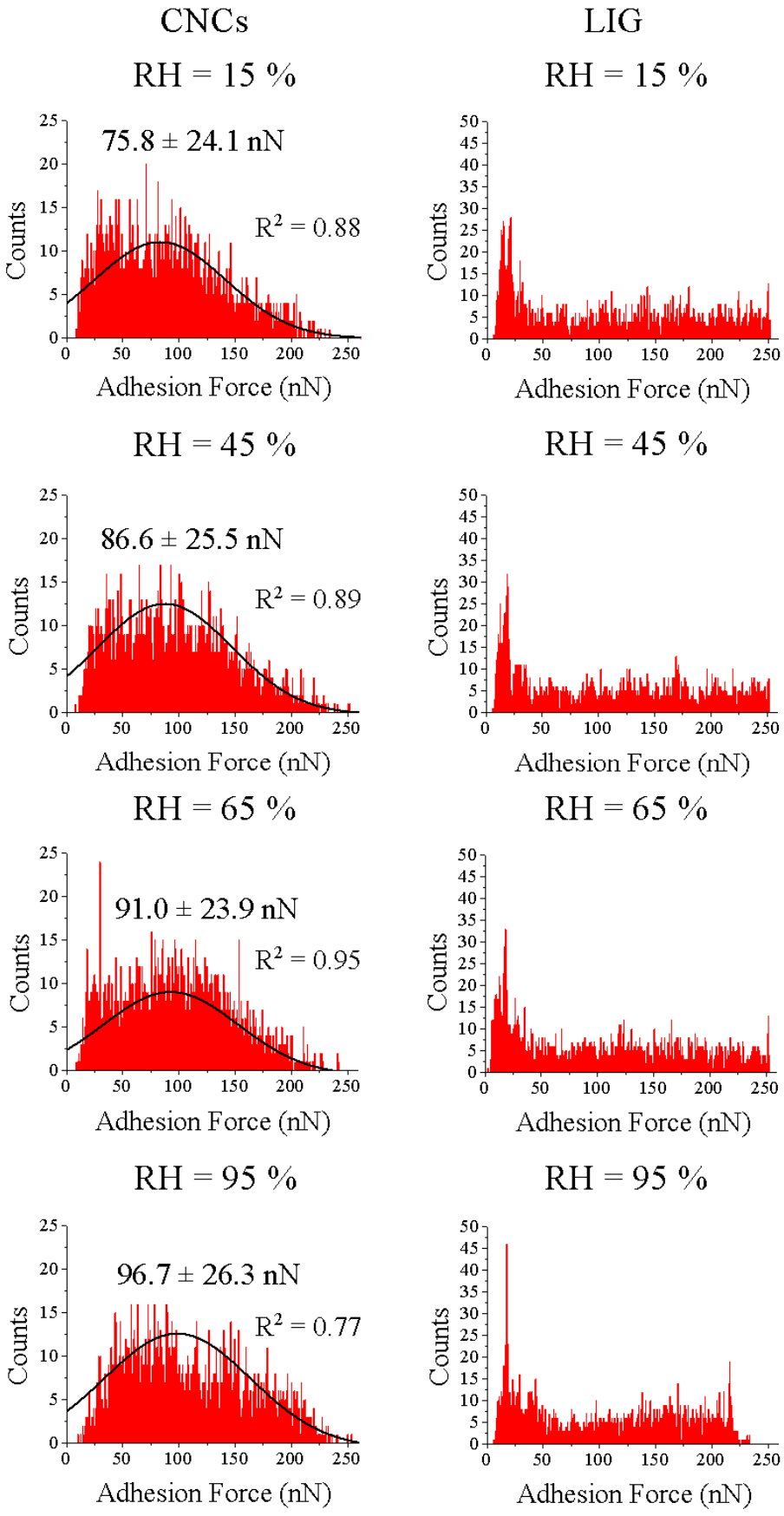

Int. J. Biol. Macromol. Carlos Marcuello and Michael Molinari. Fig. SI 7

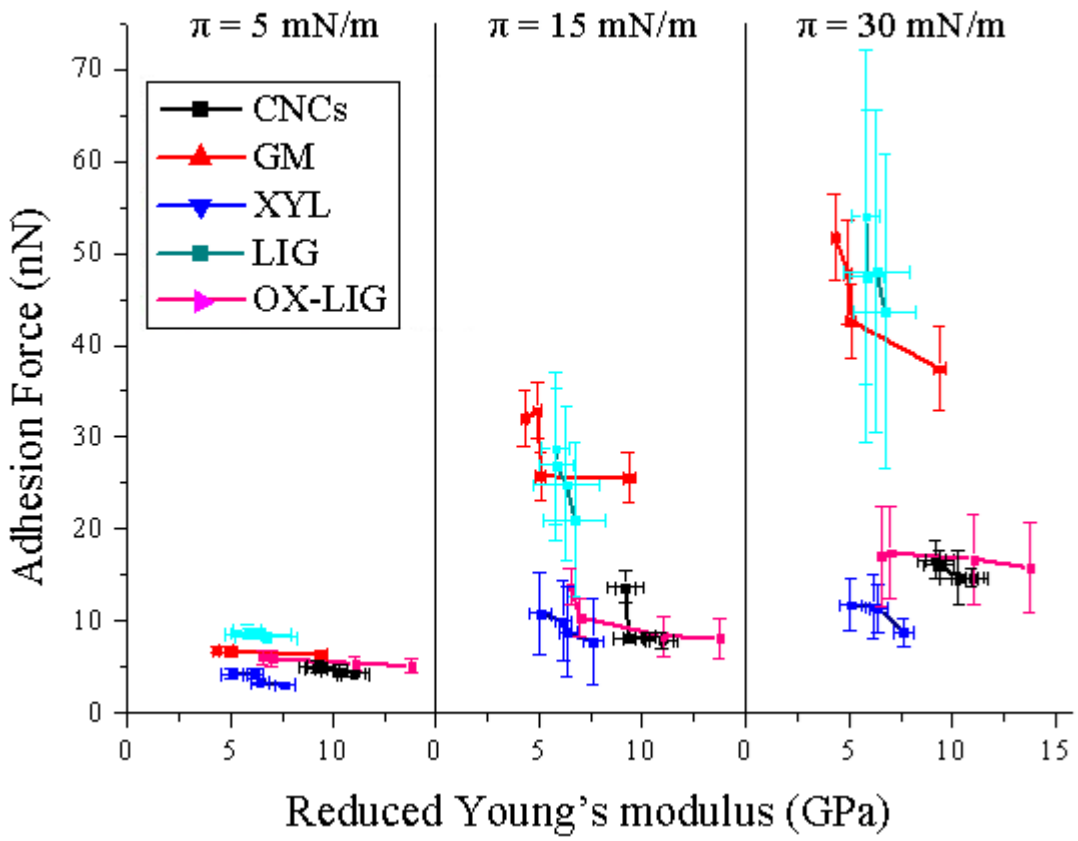

Int. J. Biol. Macromol. Carlos Marcuello and Michael Molinari. Fig. SI 8